Chapter 3 Sand Motion near the Sand Bed Surface

Under the direct action of aerodynamic forces, a portion of sand particles on the bed tend to roll and slide forward, which is called creeping, while some particles tend to lift off the sand bed with certain velocities, and then act as saltation or suspension. The creeping particles are likely to excite their neighboring particles to jerk up into the air, and the saltating ones, after falling back to the ground, are likely to rebound and eject several of their neighboring particles out of the bed. Such lift-off and splash processes taking place near the sand bed are a significant ingredient of wind-blown sand movement, they directly influence the trajectories of sand particles and the development of wind-blown sand flow, and they always serve as the initial conditions for theoretical prediction models of sand motion.

As we can imagine, the scale and dominating physical rules of a single particle's motion may be different in essence from those of wind-blown sand movement which involves a countless number of moving sand particles. In the view of a single particle's motion, too many variables are involved to simulate the wind-blown sand movement process, which makes it an absolutely formidable challenge to take the initial lift-off value of every sand particle into the equations of motion, even with a supercomputer. Therefore, when dealing with such multi-scale problems, we always need to draw lessons from the statistics. Similar to the roles the Avogadro and Boltzmann constants played in describing the properties of molecular motion and ideal gas respectively (Feynman 1963), it is necessary to introduce the probability density function (PDF) of lift-off velocities and the splash function as key statistical quantities to connect the two physical phenomena of different scales, i.e., the micro-scale motion of a single particle and the macro-scale behavior of the windblown sand movement process. The determination of the PDF of lift-off velocities and the splash function is always based on the analysis of the interaction between sand particles and the bed. Therefore, the content of this chapter is arranged as follows, Sect. 3.1 introduces the threshold wind velocity for sand entrainment; Sect. 3.2 presents the results of existing observations on particle-bed

X. Zheng, *Mechanics of Wind-blown Sand Movements*, Environmental Science and Engineering,
DOI 10.1007/978-3-540-88254-1_3, © Springer-Verlag Berlin Heidelberg 2009

collision processes and lift-off velocities of sand particles; Sects. 3.3 and 3.4 provide a theoretical model based on the stochastic particle-bed collisions to obtain the PDF of lift-off velocities and some numerical methods to obtain the splash function, respectively.

3.1 Threshold Wind Velocity for Sand Motion

3.1.1 Mechanism of the Entrainment of Sand Particles

The entrainment mechanism of sand particles is an important research subject in the study of wind-blown sand movement. From experiments, we can observe that it is a complex micro-process in which sand particles dislodging from the sand bed and move downstream under the wind force. When wind velocity reaches a certain level, a few protuberant particles begin to vibrate or swing backwards and forwards without leaving a stationary position under the influence of turbulence and pressure fluctuations. As wind velocity increases up to some threshold value, the amplitude and frequency of sand vibration, the frontal resistance $\mathbf{F}_D$ (i.e., the drag force) and the lifting force $\mathbf{F}_L$ acting on a sand particle increase accordingly to overcome the gravitational force $\mathbf{F}_g$, which produces a large rotary moment, and hence results in some most susceptible sand particles rolling and sliding downwind. Because of the irregularity of a sand particles' shape, the diversity of sorting and packing, and variation in the acting forces, some rolling particles will collide with those protuberant ones resting on the bed or be impacted by other moving ones. In this way, they rapidly attain enough momentum to change the motion downwind into motion upward. After a transient moment of collision, such rapid change leads these particles to lift off the bed and become saltated in the airstream.

There have been several different arguments on the entrainment mechanism of sand motion. Based on wind tunnel observations, Bagnold (1941) regarded that the initial dislodgement occurs under the direct effects of wind forces when the wind velocity rises to some threshold value, which he called the fluid threshold. Afterwards Bagnold (1941) also suggested that the initial dislodgement may result from collision of saltating particles, and named the minimal wind velocity required to maintain the sand movement as the impact threshold velocity. However, Exner and Hampe (1953) concluded that the dislodgement of sand particles is a result of turbulent diffusion while Von Karman (1956) and Lyles and Krauss (1971) also found that the vertical fluctuation of turbulence plays a significant role in lifting sand particles from the bed. They argued that the turbulent shear

stress is always larger than the laminar shear stress, and the maximum fluctuation of airflow accounts for about 15% of the average value, so turbulence obviously performs a key activation role on the entrainment of sand particles. Nevertheless, there're still other different views on the effect of the turbulence. For example, Bagnold (1941) regarded that the effect of turbulence works only when the wind velocity is high enough, which therefore means he thought the turbulence is not the main reason for the entrainment of particles. Until now, there have been more than 8 different theoretical hypotheses concerning the mechanism of the entrainment of sand particles, which can be categorized into 2 groups, namely the contact force entrainment hypothesis and the non-contact force (aerodynamic force) hypothesis. The former includes the inclined flying hypothesis, the saltating impact hypothesis, and the vibration hypothesis; the latter includes the buoyancy force hypothesis, the aerodynamic drag hypothesis, the turbulence hypothesis, the negative pressure hypothesis and the vortex hypothesis. In summary, the complexity of the shape of sand particles and the configuration of sand packing make all of these coexisting hypotheses seem reasonable for the entrainment of sand particles.

3.1.2 Threshold Wind Velocity of Sand Motion

As far as the threshold wind velocity of sand motion is concerned, Bagnold (1941) showed that there are two thresholds for saltation: the fluid threshold, which is defined as the wind velocity at which particles start moving due to the action of wind only, and the impact threshold, which is defined as the wind velocity at which the combined action of wind forces and saltation impacts can just sustain sand movement, or alternatively, the wind velocity at which the energy received by saltating particles from the wind field can balance the energy losses when particles strike the bed. In general, the fluid threshold is of interest, and the impact threshold is 80% of the fluid threshold. Based on the balance between the frontal resistance $\mathbf{F}_D$ and the gravity $\mathbf{F}_g$, we can get an expression for the threshold friction velocity u_{*t} in the following form (Bagnold 1941):

$$u_{*_t} = A\sqrt{gD_s\frac{(\rho_s - \rho)}{\rho}}\,. \tag{3.1}$$

The threshold fluid velocity u_t at any height z can be obtained from the relationship between the friction velocity and wind velocity given by Eq. 2.30, that is,

$$u_t(z) = 5.75A\sqrt{gD_s\frac{(\rho_s-\rho)}{\rho}}\lg\left(\frac{z}{z_0}\right), \tag{3.2}$$

where, D_s is the particle's diameter, A is an empirical coefficient determined by experiment. For example, for 'uniform' sand, i.e., the diameters of sand particles lie within a certain range, it has been found that when $u_* r/\nu > 3.5$ (where $u_* r/\nu$ is the Reynolds number, ν is kinematic viscosity; r is the mean surface roughness which is of the order of the particle diameter. The critical Reynolds Number $u_* r/\nu = 3.5$ distinguishes the condition under which a surface may technically be considered either 'rough' or 'smooth'), the coefficient A in Eqs. 3.1 and 3.2 is nearly a constant, equal to 0.1 (Bagnold 1941) or, in the range 0.09–0.11 (Chepil 1945). Some other researchers argued that A is 0.12 (Zingg 1953) or some value within 0.17–0.20 (Lyles et al. 1971). For very small particles, when the critical Reynolds number $u_* D/r$ is less than 3.5, especially when the particle size falls below 0.2 mm, the value of coefficient A begins to rise and the square root law no longer holds. For natural sand particles of varied size, the fluid threshold is determined by the predominant particle size. Fig. 3.1 presents the particle size distributions of the natural dune sand sampled from the Minqin desert region of Gansu province and the eastern edge of the Tengger Desert, China.

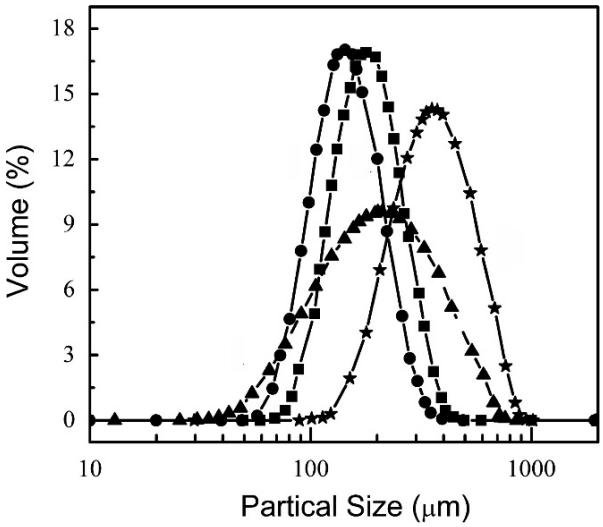

Fig. 3.1. Particle size distributions of dune sand sampled, –▲– and –★– sampled from Minqin; –●– and –■– sampled from the eastern edge of the Tengger Desert (measured by the author et al.)

From experiments conducted in a wind tunnel, we can obtain an intuitive understanding of the physical meaning of the fluid threshold and impact threshold. At the beginning stage, the flow blowing through a flat sand bed is pure wind without sand particles, and the minimum wind velocity at which sand particles begin to be dislodged is the so-called fluid threshold. As the wind velocity increases, the wind-blown sand flux begins to form. Then, if the wind velocity decreases to the fluid threshold, the wind-blown sand flux does not cease until it decreases to some value lower than the fluid threshold, which is called the impact threshold. Therefore, the impact threshold is the maximum wind velocity at which the wind-blown sand flux will cease. It can be seen that in a certain sense that these two threshold values play a similar role as the lower and upper critical Reynolds number play in the transition experiment of fluid dynamics.

3.1.3 Factors Affecting the Threshold Wind Velocity

Generally speaking, the fluid threshold velocity u_t is a piecewise function of particle diameter D_s. For 'uniform' sand, Bagnold (1941) suggested that if $D_s > 0.1$ mm, then $u_t \propto \sqrt{D_s}$, while some other experiments (Dong and Li 1998) argued that there exists a minimum threshold velocity when $D_s = 0.09$ mm. For $D_s > 0.09$ mm the motion of sand particles is dominated by inertial forces, thus u_t increases with D_s, while for $D_s < 0.1$ mm, it is dominated by cohesive force and u_t decreases with D_s. The threshold velocity of 'mixed' sand bed increases with the average sand diameter D_s, which is always lower than that of corresponding 'uniform' sand bed with the same sand diameter.

Surface conditions, such as vegetation and topography, also have an important effect on the threshold velocity through influencing the wind flow over the sand bed. Raupach et al. (1993) used drag partition theory to develop a formula for the effect of vegetation on the threshold velocity:

$$(u_{*t})_V = u_{*t}\sqrt{(1-\sigma_V\lambda_V)(1+\gamma_V\beta_V\lambda_V)} \tag{3.3}$$

where u_{*t} and $(u_{*t})_V$ are the threshold friction velocities for a bare-soil surface and a vegetated surface; λ_V is the roughness density or the frontal area index of the roughness; σ_V is the basal-to-frontal area ratio; γ_V is a parameter accounting for spatial non-uniformity in the surface stress, which equals 1 for uniform stress and decreases as non-uniformity increases; and $\beta_V = C_R / C_S$, where C_R is the drag coefficient for isolated roughness elements and C_S is that for the soil surface. Measurements results of the threshold friction velocity by Gillette and Stockton (1989) and Musick and

Gillette (1990) agree well with Eq. 3.3 when $\beta_V \approx 100$, $\gamma_V \approx 0.5$, and $\sigma_V \approx 1$. The effect of topography lies in the influence of surface slope which makes the threshold of sand particles resting on an upslope larger, and those on a downslope smaller than on a flat surface. Howard (1977) deduced a relation between the threshold velocity and the surface slope, that is,

$$(u_{*_t})^2 = \frac{\rho_s}{\rho} BD_s g\left(\tan^2 \vartheta \sin\alpha - \sin^2 \chi \sin^2 \alpha^{1/2} - \cos\chi \sin\alpha\right), \tag{3.4}$$

where $B = 0.31$ and is a dimensionless constant; α is the angle of internal friction; θ is the surface slope angle; and χ is the angle between the wind direction and the normal line of the bed surface. This relation agrees well with the results of Hardisty and Whitehouse (1988) who conducted a field observation on sand dunes in the Sahara desert with a portable wind tunnel.

In addition, surface moisture is also an important variable in controlling the entrainment processes because of the cohesion produced by the tensile force between water molecules and sand particles. It was generally believed that the threshold velocities for sand particles with moisture content bear a linear relationship to the square root of surface moisture, and so adding the same quantity of moisture, the increment of the threshold velocities of sand particles with low moisture content is larger than that with high moisture content. However, some researches (Ravi and Odorico 2005; Ravi et al. 2006; Nickling and Ecclestone 1981; Nickling 1984) recently found that the threshold velocities for sand particles in arid areas do not always increase with moisture content. They explained that as the surface moisture exists in the form of hygroscopic water, the inter-particle cohesion of sand particles decreases rapidly with moisture content (Ravi et al. 2006). Since it is relatively difficult to measure the surface moisture, ambient air humidity is taken as a substitute (Ravi and Odorico 2005). Similarly, due to the cementation effect, salt content is also considered to have a major influence. Nickling and Ecclestone (1981) and Nickling (1984) have found through experiments that u_{*_t} can be more than doubled with an increment of salt contents less than 1%, which is the reason for employing polymer binder and saline as a chemical sand solidification agent.

Besides these, some other factors, such as the shape of sand particles and electrostatic force also have significant influences on the threshold of sand motion (Kok and Renno 2008), but how these factors work is still not very clear. Therefore, some field observations or wind tunnel experiments were designed to determine the threshold velocity for specific region. For instance, Bagnold (1941) conducted field observations during the sand-

storm in the Libyan Desert and the results showed that the threshold value of u_{*t} for sand with an average diameter of 0.32 mm is about 0.23 $m \cdot s^{-1}$. Other empirical conclusions suggest that for dry bare-sand surfaces, sand particles will be uplifted when the wind velocity measured at 2 m height or recorded by metrological stations reaches about 4–5 $m \cdot s^{-1}$. Though a lot of pioneering work has been done on the entrainment of sand particles, there remain some unclear problems which are related to complex factors affecting the entrainment of sand particles. Therefore, these factors are still an important subject in the study of wind-blown sand movement until now.

3.2 Experimental Research on the Lift-off of Sand Particles

As we mentioned above, the velocities of sand particles lifting off the bed are significant initial conditions for predicting their trajectories in wind-blown sand movement. The most intuitive method for obtaining the lift-off velocities of sand particles is to observe the particle-bed collision process directly and capture the moment the sand leaves the bed. Such measurements can be divided into two types: laboratory experiments with 'artificial' sand and wind tunnel experiments with natural sand.

3.2.1 Experiments on Particle-Bed Collision with 'Artificial' Sand

Particle-bed collision processes have been studied since 1985 by direct observation on 'artificial' sand particles, such as steel spheres and spherical plastic beads. For example, Mitha et al. (1986) studied the direct collision of steel beads on a three-dimensional (3-D) packing of 60,000 steel beads. Both particles on the bed and the impacting particles were 4 mm steel spheres. The phenomenon was recorded through stroboscopic photography. Their results essentially confirmed the previous studies and supported Rumpel's (1985) hypothesis about the amplification mechanism of the vertical speed at low angles. Francöis et al. (2000) conducted experiments to study the collision process of particles on a two-dimensional (2-D) granular bed with identical plastic beads. These experimental researches provide some meaningful results. For example, the incident bead does not affect the bottom of the bed when the height of the packing is of 6 layers or more; while the number of ejections is enhanced at low packing height. Moreover, the ejected particles come essentially from a local region surrounding the impact point of the collision; however, in some cases, parti-

cles can be ejected from a location which is far from the impact point. Furthermore, beads ejected from a point located in front of the impact position jump forwards whereas those ejected from a point behind the impact position move backwards. The ejected particles are much less energetic than the impact particle. The number of ejected particles almost linearly increases with the impact velocity. Also, 94% of high speed impact particles will rebound from the bed and the vertical component of rebound speed increases with impact angle, and so on. However, there are still some limitations for these 'artificial' particle experiments when their results are applied to explain natural wind-blown sand movement for the following reasons: (1) the material and surface curvature of particles do have a direct influence on the particle-bed collision process; (2) there might be scale effects in substituting the sand particles of smaller scale with particles of larger scale.

3.2.2 Measurements of the Linear Velocities of Lift-off Particles

The apparatus for a wind tunnel experiment on particle-bed collisions with natural sand is showed in Fig. 3.2. When wind blows over the sand bed, particle-bed collision processes and the trajectories of saltating sand particles can be captured by high-speed camera or stroboscope. The motion of sand particles in the saltation layer is usually identified at the height of 5 mm because of the dense concentration of sand particles below 5 mm. The lift-off velocity of a certain particle can be obtained through the following manner: firstly, arbitrarily select two points, like point 2 and point 3 in Fig. 3.3, along the trajectory, which are denoted by (x_2, z_2) and (x_3, z_3), respectively; then record the time the particle takes traveling from point 2 to point 3; and finally take the average velocity $\overline{V}$ as the lift-off velocity V. The components of V can be express as:

$$V_x = \frac{1}{\Delta t}\left(x_3 - x_2\right), \quad V_z = \frac{1}{\Delta t}\left(z_3 - z_2\right). \tag{3.5}$$

As we can see, the lift-off velocities of sand particles obtained in this manner are obviously not accurate enough. Therefore, the lift-off velocity can also be inversed by substituting the coordinates of point 2 and point 3 into the trajectory equations on the basis of a theoretical model of particle motions. It is notable that it's difficult to obtain the analytical solution of trajectory function if all factors influencing the trajectory of sand particle are incorporated. However, on the other hand, oversimplification weakens the accuracy of lift-off velocity.

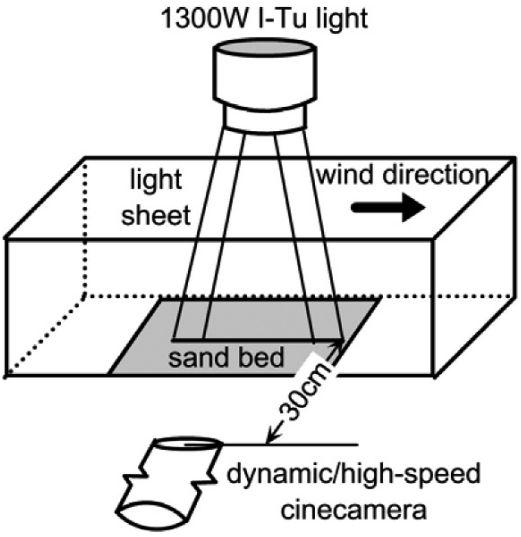

Fig. 3.2. Schematic diagrams of apparatus of wind tunnel experiment on particle-bed collision; 1300W I-Tu light is used to present a light sheet about 1 cm in thickness and dynamic/high-speed cinecamera is put outside of wind tunnel, 30 cm away from the wind tunnel

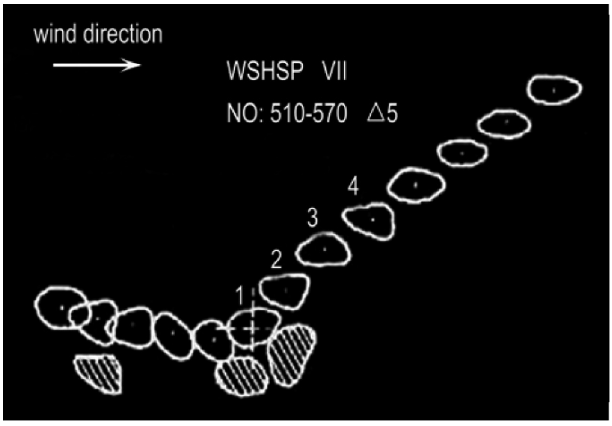

Fig. 3.3. Trajectory of a sand particle captured by high-speed camera and the number 1–4 denotes each position of a sand particle for 4 continuous photographs (from Xie et al. 2007)

Although high-speed cameras and stroboscopes are advantageous to capture continuous images of sand motions in time and space, it's difficult to differentiate the sand particles in a dense packing layer, which restricts

the height of measurement to 5 mm or higher above the sand bed (White and Schulz 1977; Zou et al. 2001). Moreover, judging experimental results by naked eyes restrains to some extent the number of sampling and the degree of accuracy. Recently, Phase Doppler Anemometry (PDA) and Phase Doppler Particle Analyzer (PDPA), in which the laser holographic technology is employed, are used to measure velocities of sand particles in the wind-blown sand flux. For example, Dong et al. (2002) used PDA to detect the saltation of size-sieved sand particles at different friction velocities in a wind tunnel, and presented the statistical results of the incident velocities, the lift-off velocities, the incident angles and the lift-off angles of the particles. Although it has the capability of analyzing a great deal of samples with the aid of computer, PDA technique is weak in determining the diameter of sand particles and in detecting the whole-field information. Besides, single-point PDA measurement fails to reflect the influence of varying measuring height resulting from the erosion or accumulation of sand bed in the wind-blown sand flux.

Based on the speckle technique, which has been applied to measure the strain-displacement of solids, the methods of Particle Image Velocimetry (PIV), and the Particle Tracking Velocimetry (PTV) algorithm (Dabiri and Ghairb 1991; Delnoij et al. 2000), can be used together to reveal the position, movement and diameter of sand particle in wind-blown sand flux. Compared with the PDA technique, PIV breaks through the space limitation of single-point measurement. It not only has the high accuracy and resolution of existing single-point measurement, but also the ability to obtain a fast and non-intrusive measurement and instantaneous image of entire flow fields. The measurement of the motion of sand particles in an wind-blown sand flux with a PIV system works like this: A dual laser is employed to provide a light sheet, an image capture device (i.e., a CCD Camera) is used to capture the flow field and sand particles passing through the light sheet. PIV images are gray level images. The position of sand particle is determined by image processing technique. The velocities of sand particles are obtained by measuring the distance each particle travels in a fixed time interval, a pair of pictures is captured by PIV to locate the particle and a cross-correlation algorithm is used to match the particles.

The procedures for acquiring the information of particle movement from these images are divided into three steps: the threshold segregation, locating particles and correlative particle matching. In the first step, as the gray level of irradiated particles is significantly larger than the dark background, they could be segregated from the background with certain thresholds of gray level. The pixels whose gray levels are larger than the threshold are assigned as 1, and those smaller than the threshold are assigned as

0. The gray level threshold is calibrated after a comparison of the calculated distribution of diameters and the distribution of the sand bed after the second step.

With the two-value image obtained in the first step, it is relatively easy to detect the edge of each particle area with an edge algorithm (Gonzalez and Woods 2003). Counting the number of pixels occupied by each particle and locating the center of each particle, we can calculate the diameters of sand particles by assuming that the shape of sand particle is a sphere and its cross-section is a circle.

In the last step, the cross-correlation algorithm is used to match correlative particles on a pair of PIV images captured within a certain time interval, thus we can get the displacement that the particle traveling in a certain interval of time, or its velocity vector. As there are particles in the first one of a pair of PIV images with large lateral velocity, they might not be captured in the second exposure, thus the cross-correlation algorithm could not match the image of the same particle in two frames, or matches the wrong pairs of particles. A threshold of correlative coefficient should be set to judge the matching of particles and eliminate pseudo-vectors. Finally, the position, speed and diameter of sand particles in a transient of wind-blown sand flow are obtained. Fig. 3.4 shows one of the results of image processing of PIV images of sand particle within 1.3 cm above the sand bed.

Through this method, we could obtain the distribution of lift-off velocities by referring to the sand particle near the sand bed with positive vertical velocity as the lift-off particle or by applying the trajectory equation to figure out the instantaneous lift-off velocity. The advantage of a PIV system make it possible to measure the diameter and the velocities

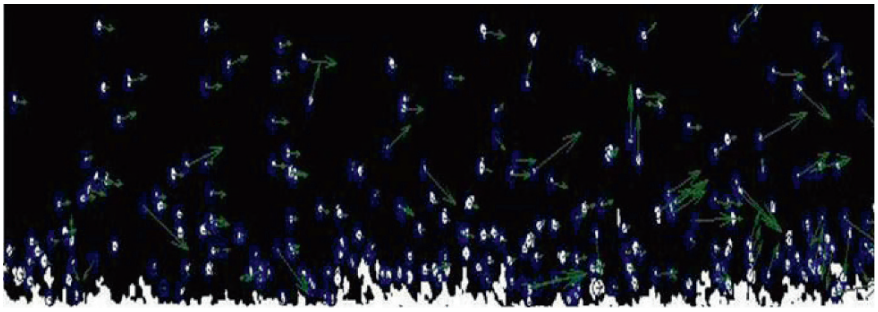

Fig. 3.4. The results of image processing of a pair of PIV images of sand particles within 1.3 cm above the sand bed, in which the hollow circles and arrows represent respectively the position and velocity vector of each sand particle. (photo by the author et al. in Multi-function wind tunnel of Lanzhou university)

of sand particles instantaneously, and therefore to study the affect of wind velocity and particle diameter on the entrainment of saltating sand particles. The preliminary result of wind tunnel experiment based on PIV show that, at certain wind velocities, the lift-off velocities of sand particles increase as their diameters decrease and the lift-off velocities of sand particles with a certain fixed diameter increase as the wind velocity increases.

Furthermore, wind tunnel experiments of particle-bed collision reveal that most sand particles lift-off along the wind direction, the rebound angle is roughly 40°– 60° and the rebound speed is roughly 50%–60% of pre-impact value, the ejection speed of splashed sand particles are of the order of 10% of the impact velocity, and the number of splashed sand particles is usually 2–10 (Willetts and Rice 1986; Rice et al. 1995). High speed impact sand particles may continously rebound 19–20 times, but if the bed is perfectly rigid, the rebounding particle would most likely emerge from the collision at an angle of 30°–50° (Anderson et al. 1991).

Directly measuring the transient lift-off velocities of sand particles is still an open problem at present. The sampling frequencies and resolutions of current instruments are restricted by the processing speeds and memory capacities of both the computer and the camera. Continuous whole field measurement of wind-blown sand flow is not possible yet. An ideal high-speed sampling method might trace the path of each sand particle in the whole field while measuring the diameter and speed of each particle so as to provide an accurate prediction of the lift-off velocity.

3.2.3 Measurement of the Angular Velocities of Saltating Particles

The angular velocity of a saltating particle is a key quantity to determine the Magnus force, which affect the trajectory of a sand particle and the profile of mass flux. It can be obtained by analysing the trajectory and counting the number of twist of the trajectory. The mean lift-off angular velocity was 200–1000 rev·s^{-1} (Chepil and Woodruff 1963; Tanaka and Kakinuma 1960). Ewannouve (1972) regarded that the lift-off angular velocity was 100–600 rev·s^{-1} for particles with diameters larger than 0.2 mm, 400–600 rev·s^{-1} for particles with diameters of 0.15–0.2 mm. Rice et al. (1995) found that the lift-off angular velocity was 430–850 rev·s^{-1} for particles with diameters of 0.425–0.6 mm and incident angular velocities of 300–670 rev·s^{-1}.

Recently, some new results have been obtained on saltating sand particles' angular velocities through laboratory measurement (Xie et al.

2007). The experiment was conducted in a blow-type, noncirculating wind tunnel. The sand particles employed in the experiment were natural quartz sand particles, which are usually not round and whose diameters range from 0.25 mm to 1.5 mm and the mean diameter is 1.0 mm. The sand particles were laid on the bed with a thickness of 5 cm in the tunnel. A 1300 W high color-temperature I-Tu lamp (LSY 220-1300) light source was mounted 30 cm above the sand bed. A high-speed (HEPING, 35 $f \cdot s^{-1}$) and a dynamic cinecamera (PENTAZET-ZL1-35) were set to take photos of saltating particles. Figs. 3.5a and 3.5b are two of the photos that were

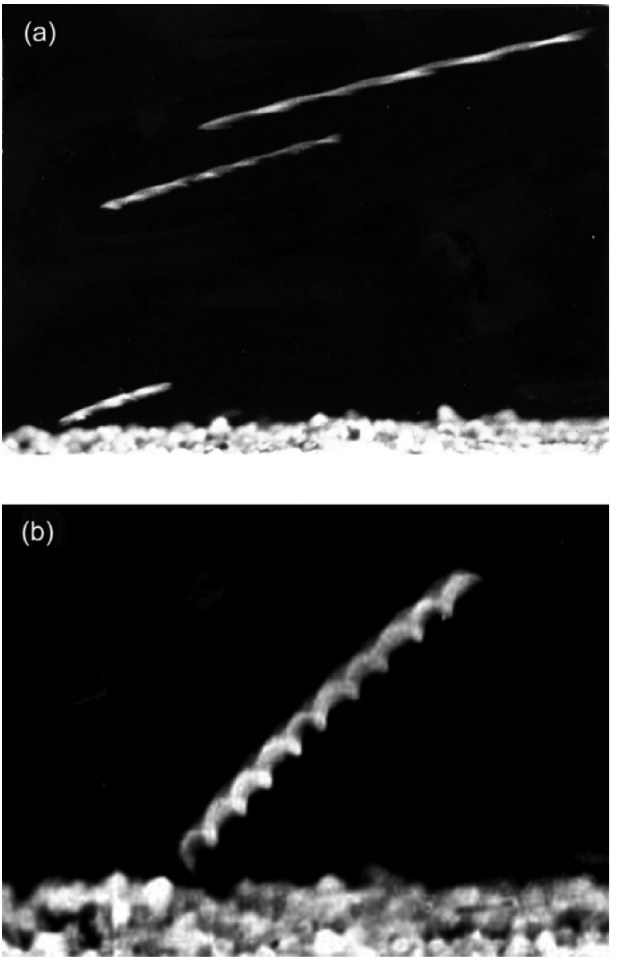

Fig. 3.5. Two basic spin patterns captured by dynamic cinecamera **(a)** in-plane spin, the rotation axial prallel with the linear velocity, and **(b)** out-plane spin, the rotation axial perpendicular to the linear velocity (from Xie et al. 2007)

taken by the dynamic cinecamera, in each of which a segment of trajectory of a saltating particle is captured. From the spiral shape of the trajectory in Fig. 3.5a, we can easily make out that the particle's spin axis is in the plane of the light sheet and verticle to the sand bed, and we name this spin pattern as an in-plane spin. The spin axis of the trajectory segment in Fig. 3.5b is vertical to the plane of the light sheet, which is named as out-plane spin. In general, the value and distribution of spin speed are different for the two kind of spin pattern, and in-plane spin is the major pattern.

Furthermore, from the photos captured by the dynamic cinecamera, we can easily recognize two kinds of in-plane spin, as shown in Fig. 3.6.

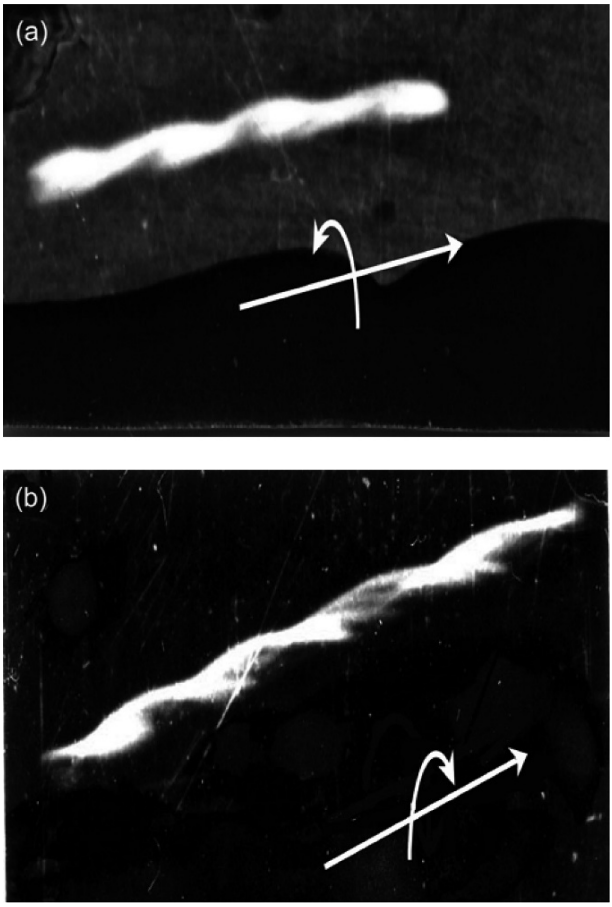

Fig. 3.6. Two patterns of in-plane spin. **(a)** left spin and **(b)** right spin, in which the straight arrows represent the translation directions of the sand particles and the curved arrows indicate the rotation directions (from Xie et al. 2007)

Table 3.1. Out-plane angular velocities at different stages of saltation trajectory

Angular velocity [Rev·s^{-1}]	Lift-off	Ascending flight	Descending flight	Impact
Mean value	344	348	254	167
Maximum value	896	1088	784	448
Minimum value	64	64	64	64

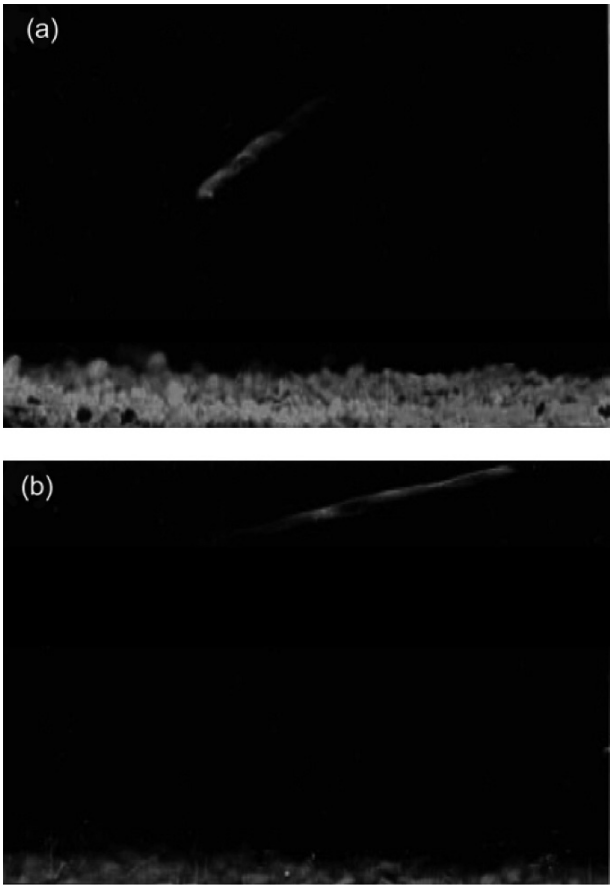

Fig. 3.7. Two unclear parts of saltation trajectories: **(a)** the tail is not clear and **(b)** the head is not clear, which maybe mean that the sand's trajectory is not in the light sheet (from Xie et al. 2007)

Keeping thumb pointing in the direction of movement, the direction of spin is left-handed in Fig. 3.6a and right-handed in Fig. 3.6b, which are left spin and right spin, respectively. The out-plane spin angular velocity rangs

from 0 to 1088 rev·s^{-1} and varies in its entire flight process, as shown in Table 3.1. It can be seen that sometimes the maximum value of out-plane rolling angular velocities may reach 1088 rev·s^{-1} and its minimum value as low as 64 rev·s^{-1}, the angular velocity increases in the ascending flight of a sand particle and then decreases in its descending flight, and usually the impact angular velocity is lower than the lift-off angular velocity.

A very interesting result observed from the experimental photos is that some segments of trajectories are not clear, especially at the heads or the tails, as shown in Fig. 3.7. It is very possible that the segment is a part of a 3-D saltation trajectory. More studies are needed to verify whether the Magnus forces arising from spin make the sand particles' trajectories deviate from the 2-D plane.

3.3 Stochastic Model of Particle-Bed Collision

With the experimental method mentioned above, the lift-off velocities of sand particles and thus the probability density function of lift-off velocities can be obtained. However, there are some inherent limitations of the experimental measurement. For example, when the concentration of sand particles is very dense, the size of sand particles is too fine to be identified, or if the bed surface is very rough, the initial motion of the sand particles cannot be directly measured by experiment even with the most advanced equipment such as PIV or PDA. Besides, the accuracy of inverse calculation of the lift-off velocities through juding the position, motion or path of each particle in photographic images depends on the establishment and solution of the trajectory equations of sand motion. Therefore, modelling the particle-bed collsion process from collision mechanics has intensified as an important tool to investigate the lift-off velocities of sand particles and to remedy the deficiency of experimental method. Here, we introduce a so-called stochastic particle-bed collision model which can further reflect the real particle-bed process compared with previous models.

3.3.1 Stochastic Model

For simplicity, we deal with the sand particles in the collision as two-dimensional (2-D) circular disks and an effective model of the real collision is given in Fig. 3.8 (Zheng et al. 2005, 2006). In order to describe this collision in Fig. 3.8, we take the representative particles A and B to indicate the descending particle and the creeping particle, respectively.

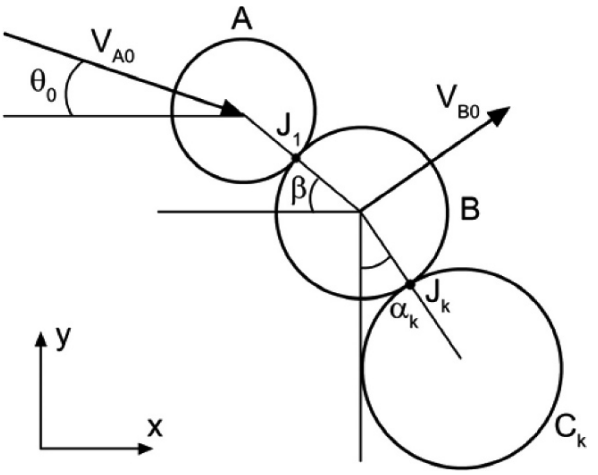

Fig. 3.8. Schematic drawing of the collision of descending particles with the sand bed at instant of the collision beginning. *A* and *B* are the descending particle and the creeping particle. V_{A0} and angle θ_0 are the incident velocity and incident angle. β is the impact angle and α_k is the contact angle. J_1 and J_k are the contact points between the incident sand and the creeping sand, and the creeping sand and sustain sand (from Zheng et al. 2005)

Assume that the particle *A* has an equivalent diameter of D_A, mass of m_A and descending velocity of magnitude V_{A0} and angle θ_0 from the horizontal, which collides with particle *B*. Particle *B* has an equivalent diameter of D_B, mass of m_B and velocity of V_{B0}. In contrast to previous particle-bed collision model (Werner 1988; Anderson and Haff 1991), we introduce an effective sand particle C_k, which has an equivalent diameter of D_k and mass of m_k, to reflect the resultant actions on the particle *B* by other *k* ($k = 1, 2, \ldots$) sand particles on the sand bed. We denote the contact point between the particles *A* and *B*, and the particles *B* and C_k by J_1 and J_2, respectively. In addition, we introduce two angle parameters called contact angle α_k and impact angle β to characterize the orientation of the lines connecting the centers of particles (see Fig. 3.8).

Another important difference between the stochastic particle-bed collision model and previous particle-bed collision model is to reflect the randomness of particle-bed collision processes, the diameter and mass of sand particle, the incident velocity V_{A0}, the creeping velocity V_{B0}, the incident angle θ_0, the impact angle β as well as the contact angle α_k are all treated as random variables. In order to give the range of these random variables, it is necessary to analyze the probability distribution functions (PDFs) of these variables. According to the experimental observations of the particle-

bed collision process, the incident velocity V_{A0}, the creeping velocity V_{B0} and the impact angle β can be considered as independent variables. From observations using high speed cine-film, the sand particles on the sand bed are stationary or vibrate at a low speed of about 0–2.0 m·s^{-1} (Wu 1985) when the wind velocity approaches 18 m·s^{-1}. Because the probabilities of sand particle moving downwind and upwind are equal, here a linear probability distribution function (PDF) is selected to approximate the PDF of creeping velocity, which is

$$f_{V_{B0}} = \begin{cases} -\frac{1}{4}V_{B0} + \frac{1}{2} & 0 \le V_{B0} \le 2.0 \\ \frac{1}{4}V_{B0} + \frac{1}{2} & -2.0 \le V_{B0} \le 0 \end{cases}. \tag{3.6}$$

From the experimental data measured by Dong et al. (2002), the probability density of the incident velocity approximately fits to the gamma density function

$$f_{V_{A0}} = \frac{1}{\Gamma(\lambda_1)}\lambda_2 (\lambda_2 V_{A0})^{\lambda_1 - 1} \exp(-\lambda_2 V_{A0}), \tag{3.7}$$

where λ_1, $\lambda_2 > 0$, $V_{A0} > 0$, and λ_1, λ_2 are the parameters determined by the mean value and the variance of experiment data (see Xie et al. 2005), $\Gamma(\cdot)$ is the gamma function. Based on the measurement results of Rumpel (1985), we assume $\theta_0 \le \pi/2$, and the impact angle β is not greater than $(\theta_0 + \pi/2.0)$. In this case, the impact angle β lies in a range of $(\theta_0, \theta_0 + \pi/2.0)$. When $\theta_0 \le \pi/2$, namely the collision happens in the lee side of particle B, we find that β lies in the range of $(\theta_0 - \pi/2.0, \theta_0)$ with similar reasoning. When the incident angle is given, the conditional PDF of the impact angle is expressed as

$$f_\beta(\beta \mid \theta_0) = \frac{2}{\pi}. \tag{3.8}$$

As far as the range of contact angle α_k is concerned, it is related to the pattern of sand particles in the sand bed, the incident velocity V_{A0} and the incident angle θ_0. For simplicity, we suppose that the α_k be uniformly distributed in $(-\pi/2, \pi/2)$ although it is still worthy of further discussion. Then the probability distribution function of the contact angle is written as

$$f_{\alpha_k} = \frac{1}{\pi}. \tag{3.9}$$

After modeling the particle-bed collision process with the stochastic particle-bed collision model, we have to deal further with the collision between the particle A and B, so as to obtain the lift-off velocities of particles after collision. As we know, the collision problem has been widely studied in theoretical research and engineering application, however, the complexity of the collision process and the diversity of influencing factors make it still a significant field of mechanics (Nikolai et al. 2007; Belai et al. 2007). For the collision of two particles, several mechanical models have been put forward to simulate the collision process, which can be classified into the soft-particle approach and the hard-particle approach, depending on whether the deformation of the particle during the collision process is considered or not. Here, we briefly introduce the two approaches.

3.3.2 Soft-Particle Approach for Collision Process

The Discrete Element Method (DEM) was developed by Cundall and Stack (1979) and has been extended and applied in granular systems (Tsuji et al. 1993; Mikami et al. 1998). Werner and Haff (1988) introduced the DEM to simulate the particle-bed impacts in wind-blown sand flux. In the soft-particle approach, particle-particle interaction is usually modeled by using a spring, dash-pot and slider as shown in Fig. 3.9, in which the spring and dash-pot are employed to reflect the deformation and damping during contact, and slider is used to reflect the slip friction. If the diameter of one of the two particles is taken as infinity, then this model can be used to treat the collision between a particle and a wall. Here, we will only take the two-dimensional case to illustrate how to determine the lift-off velocities of sand particles after collisions in wind-blown sand flux by the soft-particle approach.

A rectangular coordinate system Oxz is established, with the x axis parallel to the wind flow direction and the z axis perpendicular to the bed surface and pointing upward. The neighboring particles in direct contact with particle B (x_B, z_B) during the collision process are j (x_j, z_j) (j = 1, 2, ... , N). The forces acting on B include the gravitational force $\mathbf{F}_{gB} = m_B\mathbf{g}$, the normal contact force $\mathbf{F}_{pn}^{Bj}$, the tangential friction force $\mathbf{F}_{ft}^{Bj}$, and the normal and tangential damping forces $\mathbf{F}_{m}^{Bj}$, $\mathbf{F}_{rt}^{Bj}$, which are respectively assumed to be proportional to both the normal and tangential displacements of particle j, and to the rate of change of the distance between centers of colliding particles. By resolving the above forces for the x and z axis, equations for the motion of particle B can be formulated as follow

$$\sum_{j}^{N}\left(\mathbf{F}_{pn}^{Bj}+\mathbf{F}_{ft}^{Bj}+\mathbf{F}_{rn}^{Bj}+\mathbf{F}_{rt}^{Bj}\right)_{x}=m_{B}\frac{d^{2}x_{B}}{dt^{2}}, \tag{3.10}$$

$$\sum_{j}^{N}\left(\mathbf{F}_{pn}^{Bj}+\mathbf{F}_{ft}^{Bj}+\mathbf{F}_{rn}^{Bj}+\mathbf{F}_{rt}^{Bj}\right)_{z}-m_{B}g=m_{B}\frac{d^{2}z_{B}}{dt^{2}}, \tag{3.11}$$

$$\sum_{j}^{N}\left[\mathbf{r}_{Bj}\times\left(\mathbf{F}_{ft}^{Bj}-\mathbf{F}_{rt}^{Bj}\right)\right]=I_{B}\frac{d\boldsymbol{\omega}_{B}}{dt}, \tag{3.12}$$

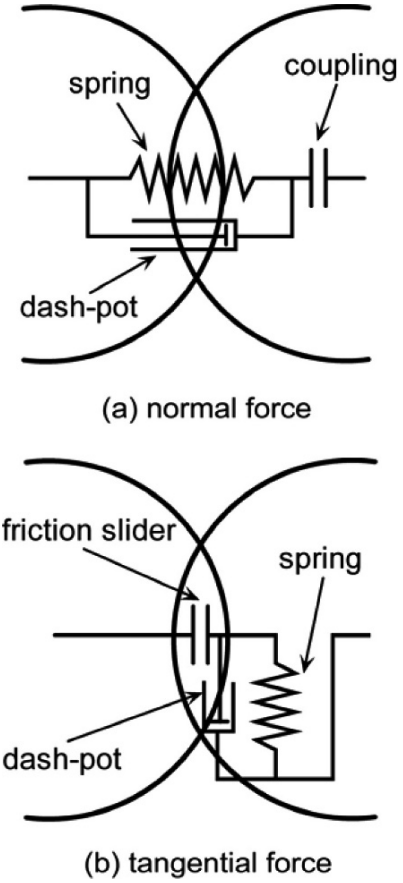

Fig. 3.9. Schematic view of the contact forces in the linear spring damping contact model, and **(a)** shows the normal force and **(b)** shows tangentical force between two collision sand particle

The initial condition for particle B can be written as:

$$t = 0:\ x_B = x_{B0},\ z_B = z_{B0},\ \frac{dx_B}{dt} = V'_{B0x},\ \frac{dz_B}{dt} = V'_{B0z},\ \omega_{B0} = 0. \qquad (3.13)$$

Where I_B is the inertia moment of particle B about its center of mass, ω_B is the angular velocity, $\mathbf{r}_{Bj}$ is a vector running from the centre of the particle B to the contact point of particle j, which can be derived from (x_B, z_B) and (x_j, z_j), and x_{B0}, $z_{B0,}$ V'_{B0x}, V'_{B0z} are initial coordinates and velocity components of particle B. Through solving Eqs. 3.10–3.13, we can get the position (x_B, z_B) and the velocity components V_{Bx}, V_{Bz} of particle B after collision, and hence the lift-off velocity V_{B0x}, V_{B0z} of B.

3.3.3 Hard-Particle Approach for Collision Process

The hard-particle approach was first put forward by Alder and Wainwright (1957) to study the phase transition for hard-sphere systems, and was latter widely applied in granular dynamics, such as the simulation of a gas-solid two-phase flow in a two-dimensional (2-D) horizontal channel (Tsuji et al. 1987), bubble and slug formation and segregation phenomena in gas-fluidized beds (Hoomans et al. 1996) and so on. In contrast to the soft-particle approach, in the hard-particle approach, particle-particle interaction is assumed to be a sequentially instantaneous two-body elastic collision without considering the deformation, overlap and collision forces of particles. Consequentially, according to the momentum conservation principle in the collision theory (Halliday et al. 1997; Chatterjee 1997), the linear and angular velocities of particles after collision can be deduced for given initial conditions.

Here, we still take the two-dimensional (2-D) case as an example. According to collision theory, a collision between two bodies can be split into two processes, compression and recovery. For particles A and B, the horizontal and vertical velocity components and the angular velocity of A and B in the compression and recovery process are respectively denoted by V'_{Ax}, V'_{Az}, ω'_A, V'_{Bx}, V'_{Bz}, ω'_B, V_{Ax}, V_{Az}, ω_A, V_{Bx}, V_{Bz}, ω_B. S'_n (S_n) and S'_τ (S_τ) stand for the impulse momentum of the interacting forces at the contact points during the compression (recovery) process, and subscripts τ and n represent the tangential and normal components of the impulse, respectively. S_1 (S'_1) and S_2 (S'_2) are the tangential and normal components of the impulse resulting from the action of the bed surface or effective particle C_k to particle B during compression (recovery) process. The impulse momentum and velocity components acting on particle A and B are shown in Fig. 3.10 (for simplicity, only the compression process is illustrated).

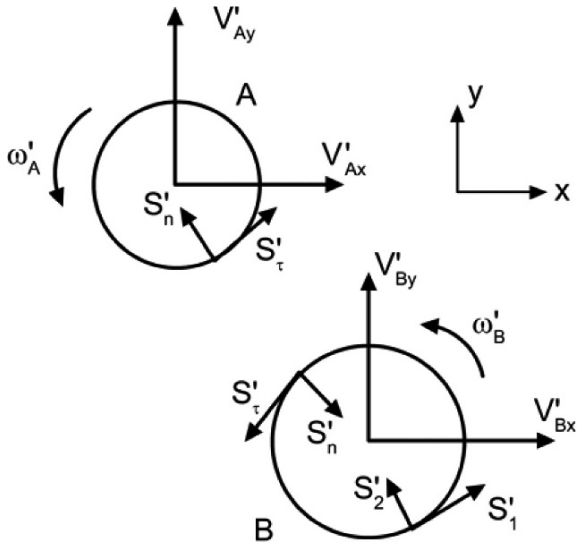

Fig. 3.10. Schematic drawing of the impulse momentum and velocity components of particle A and B; V'_{Ax}, V'_{Az}, ω'_A, V'_{Bx}, V'_{Bz}, ω'_B, S'_n and S'_τ stand for the linear velocity components, angular velocity components and impulse momentum of interact forces at contact points during compression reaching up its maximum

Therefore, the equations for the compression and recovery process of particles A and B are written as follows:

$$S'_\tau = m_A\left[V'_{Ax}\sin\beta + V'_{Az}\cos\beta - V_{A0}\sin\left(\beta-\theta_0\right)\right], \tag{3.14a}$$

$$S'_n = m_A\left[V'_{Az}\sin\beta - V'_{Ax}\cos\beta + V_{A0}\cos\left(\beta-\theta_0\right)\right], \tag{3.14b}$$

$$S'_\tau D_A = \frac{1}{4}m_A\omega'_A D_A^2, \tag{3.14c}$$

$$S'_1\cos\alpha_k - S'_2\sin\alpha_k + S'_n\cos\beta - S'_\tau\sin\beta = m_B\left(V'_{Bx} - V_{B0}\cos\alpha_k\right), \tag{3.15a}$$

$$S'_1\sin\alpha_k + S'_2\cos\alpha_k - S'_n\sin\beta - S'_\tau\cos\beta = m_B\left(V'_{Bz} - V_{B0}\sin\alpha_k\right), \tag{3.15b}$$

$$(S'_1 + S'_\tau)D_B = \frac{1}{4}m_B\omega'_B D_B^2, \tag{3.15c}$$

$$S_\tau = m_A\left[V_{Ax}\sin\beta + V_{Az}\cos\beta - V_{A0}\sin\left(\beta-\theta_0\right)\right], \tag{3.16a}$$

$$S_n = m_A\left[V_{Az}\sin\beta - V_{Ax}\cos\beta + V_{A0}\cos\left(\beta-\theta_0\right)\right], \tag{3.16b}$$

$$S_\tau D_A = \frac{1}{4}m_A\omega_A D_A^2, \tag{3.16c}$$

$$S_1\cos\alpha_k - S_2\sin\alpha_k + S_n\cos\beta - S_\tau\sin\beta = m_B\left(V_{Bx} - V_{B0}\cos\alpha_k\right), \tag{3.17a}$$

$$S_1\sin\alpha_k + S_2\cos\alpha_k - S_n\sin\beta - S_\tau\cos\beta = m_B\left(V_{Bz} - V_{B0}\sin\alpha_k\right), \tag{3.17b}$$

$$(S_1 + S_\tau)D_B = \frac{1}{4}m_B\omega_B D_B^2. \tag{3.17c}$$

Obviously, Eqs. 3.14–3.17, as a system of only 12 equations but containing 20 variables, is not closed. Therefore, some additional equations are required to solve them. Firstly, considering the joint conditions of contact points J_1 and J_2, we get the following equations:

$$V'_{Ax}\cos\beta - V'_{Az}\sin\beta = V'_{Bx}\cos\beta - V'_{Bz}\sin\beta, \tag{3.18a}$$

$$\frac{1}{2}\omega'_A D_A + V'_{Ax}\sin\beta + V'_{Az}\cos\beta = -\frac{1}{2}\omega'_B D_B + V'_{Bx}\sin\beta + V'_{Bz}\cos\beta, \tag{3.18b}$$

$$V'_{Bz}\cos\alpha_k - V'_{Bx}\sin\alpha_k = 0, \tag{3.18c}$$

$$\omega'_B D_B / 2 + V'_{Bx}\cos\alpha_k + V'_{By}\sin\alpha_k = 0, \tag{3.18d}$$

Then, from collision theory, there is some loss of energy in the collision process, which is mainly dependent on the restitution coefficients that are related to the normal and tangential relative velocities between two contact bodies. Denoting the normal and tangential restitution coefficients by k_1 and k_2, respectively and Applying the definition of restitution coefficient to the collision considered here, we have the following relations:

$$k_1 = \frac{V_{Az}\sin\beta - V_{Ax}\cos\beta - \left(V'_{Az}\sin\beta - V'_{Ax}\cos\beta\right)}{V'_{Az}\sin\beta - V'_{Ax}\cos\beta + V_{A0}\cos(\beta-\theta_0)}, \tag{3.19a}$$

$$k_2=\frac{2\left(V_{Az}\cos\beta+V_{Ax}\sin\beta-V'_{Az}\cos\beta-V'_{Ax}\sin\beta\right)+D_A\left(\omega_A-\omega'_A\right)}{2\left(V'_{Az}\cos\beta+V'_{Ax}\sin\beta\right)-2V_{A0}\sin(\beta-\theta_0)+\omega'_A D_A}, \quad (3.19b)$$

Afterwards, the linear and angular velocities of particles A and B can be deduced from Eqs. 3.14–3.19 for a given diameter and mass of particle A and B, e.g., incident velocity V_{A0}, creeping velocity V_{B0}, incident angle θ_0, impact angle β, contact angle α_k and normal and tangential restitution coefficients k_1 and k_2. It's notable that a significant advantage of these basic equations derived from the hard-particle approach is to incorporate the action of the bed surface to the particle being impacted, which essentially results from the character of the stochastic particle-bed collision model mentioned in Sect. 3.3.1.

3.3.4 Analytical Solution of Lift-off Velocity

Taking the assumption $k_1 = k_2 = k_{12}$ in the following discussion for simplicity (readers can refer to Francöis et al. (2000) and Namikas (2006) for more discussions on the restitution coefficient), the unknown variables of interest V_{Ax}, V_{Az}, V_{Bx}, V_{Bz}, ω_A and ω_B in Eqs. 3.14–3.19 proposed in Sect. 3.3.4 can be analytically solved in terms of the parameters α_k, β, V_{A0}, V_{B0}, θ_0, D_A, D_B, and k_{12}. Here, we list the solutions of the ejected and rebound velocities of sand particles with the help of Matlab:

$$\begin{aligned}V_{Ax}=&\{(\cos\alpha_k+\sin\beta)\left[\sin(\beta-\theta_0)+\cos(\alpha_k+\theta_0)+2\cos(\alpha_k+\beta)\cos(\beta-\theta_0)\right]\\&2D_A^3(1+k_{12})/D_B^3-(1+k_{12})\left[1+\sin(\alpha_k+\beta)\right]\left[\cos(\alpha_k+\theta_0)-\sin(\beta-\theta_0)\right]\sin\beta\\&4D_A^3/D_B^3+6(1+k_{12})\sin(\beta-\theta_0)\sin\beta\}V_{A0}/\{[1+\sin(\alpha_k+\beta)][2-\sin(\alpha_k+\beta)]\\&4D_A^3/D_B^3+9\}-k_{12}V_{A0}\cos\theta_0+2\left[3\cos\alpha_k+\sin\beta-2\sin\beta\sin(\alpha_k+\beta)\right]V_{B0}\\&(1+k_{12})/\{[1+\sin(\alpha_k+\beta)][2-\sin(\alpha_k+\beta)]4D_A^3/D_B^3+9\}\end{aligned} \quad (3.20)$$

$$\begin{aligned}V_{Az}=&\{(\sin\alpha_k+\cos\beta)\left[\sin(\beta-\theta_0)+\cos(\alpha_k+\theta_0)+2\cos(\alpha_k+\beta)\cos(\beta-\theta_0)\right]\\&2D_A^3(1+k_{12})/D_B^3-(1+k_{12})\left[1+\sin(\alpha_k+\beta)\right]\left[\cos(\alpha_k+\theta_0)-\sin(\beta-\theta_0)\right]\cos\beta\\&4D_A^3/D_B^3+6(1+k_{12})\sin(\beta-\theta_0)\cos\beta\}V_{A0}/\{[1+\sin(\alpha_k+\beta)][2-\sin(\alpha_k+\beta)]\\&4D_B^3/D_B^3+9\}+k_{12}V_{A0}\sin\theta_0+(1+k_{12})\left[3\sin\alpha_k+\cos\beta-2\cos\beta\sin(\alpha_k+\beta)\right]\\&2V_{B0}/\{[1+\sin(\alpha_k+\beta)][2-\sin(\alpha_k+\beta)]4D_A^3/D_B^3+9\}\end{aligned} \quad (3.21)$$

$$\begin{aligned} V_{Bx} = {} & \cos\alpha_k\left[\sin(\beta-\theta_0)+\cos(\alpha_k+\theta_0)+2\cos(\alpha_k+\beta)\cos(\beta-\theta_0)\right] \\ & 2D_B^3(1+k_{12})V_{A0}/\{9D_B^3+4D_A^3[1+\sin(\alpha_k+\beta)][2-\sin(\alpha_k+\beta)]\}+ \\ & 6(1+k_{12})V_{B0}\cos\alpha_k/\{9+4D_A^3[1+\sin(\alpha_k+\beta)][2-\sin(\alpha_k+\beta)]/D_B^3\}, \\ & -k_{12}V_{B0}\cos\alpha_k \end{aligned} \tag{3.22}$$

$$\begin{aligned} V_{Bz} = {} & \sin\alpha_k\left[\sin(\beta-\theta_0)+\cos(\alpha_k+\theta_0)+2\cos(\alpha_k+\beta)\cos(\beta-\theta_0)\right] \\ & 2D_A^3(1+k_{12})V_{A0}/\{9D_B^3+4D_A^3[1+\sin(\alpha_k+\beta)][2-\sin(\alpha_k+\beta)]\}+ \\ & 6(1+k_{12})V_{B0}\sin\alpha_k/\{9+4D_A^3[1+\sin(\alpha_k+\beta)][2-\sin(\alpha_k+\beta)]/D_B^3\}, \\ & -k_{12}V_{B0}\sin\alpha_k \end{aligned} \tag{3.23}$$

$$\begin{aligned} \omega_A = {} & 4D_A^2\{[1+\sin(\alpha_k+\beta)][\cos(\alpha_k+\theta_0)-\sin(\beta-\theta_0)]-3\sin(\beta-\theta_0)\} \\ & 2(1+k_{12})V_{A0}/\{9D_B^3+4D_A^3[1+\sin(\alpha_k+\beta)][2-\sin(\alpha_k+\beta)]\} \\ & +8(1+k_{12})[1+\sin(\alpha_k+\beta)]V_{B0}/\{9D_A+4D_A^4[1+\sin(\alpha_k+\beta)] \\ & [2-\sin(\alpha_k+\beta)]/D_B^3\} \end{aligned}, \tag{3.24}$$

$$\begin{aligned} \omega_B = {} & -\left[\sin(\beta-\theta_0)+\cos(\alpha_k+\theta_0)+2\cos(\alpha_k+\beta)\cos(\beta-\theta_0)\right] \\ & 4(1+k_{12})V_{A0}/\{9D_B+4D_A^3[1+\sin(\alpha_k+\beta)][2-\sin(\alpha_k+\beta)] \\ & /D_B^2\}-12(1+k_{12})V_{B0}/\{9D_B+4D_A^3[1+\sin(\alpha_k+\beta)] \\ & [2-\sin(\alpha_k+\beta)]/D_B^2\} \end{aligned}, \tag{3.25}$$

If the direction of wind flow and incident velocity lie in different planes, it is necessary to establish a three-dimensional (3-D) stochastic particle-bed collision model to describe the lateral component of lift-off velocities. Through solving the equations of a 3-D model, Zheng et al. (2008) deduced not only horizontal and vertical components of lift-off velocities, with the angular velocity rotating around the *x* axis (named rolling angular velocity), but also the lateral velocity, the lateral angular velocity rotating around the *y* axis and the upward angular velocity rotating around the *z* axis. Their results show that the resultant of lateral and rolling angular velocities, namely the left/right angular velocities are typically in the region of 200–300 rev·s^{-1} and the maximum value can reach up to about 1000 rev·s^{-1}, which agree well with the experimental results (Xie et al. 2007). Compared with the results of the 2-D model, it can be found that all components of both the rebound and the ejected velocities obtained by the 3-D model except the horizontal rebound velocity are lower than the corresponding ones from the 2-D model, and the differences increase with impact velocity. When the impact velocity is higher than 1.5 m·s^{-1}, the lateral

velocity is comparable with the vertical one and the lateral and upward angular velocities reach up to several revolutions per second and thus all of them cannot be ignored. Therefore, it is necessary to employ a 3-D particle-bed collision model to calculate the lift-off velocities in wind-blown sand flux.

3.4 Probability Distribution of Lift-off Velocities

The statistical distribution of velocities at which sand particles of different diameters leave the bed surface, is called the probability distribution of lift-off velocities. It describes the range of saltating particles' lift-off velocities and the probability of a sand particle rising from the bed surface with a certain velocity in wind-blown sand movement. In the theoretical prediction of wind-blown sand flux, the form of splash function and distribution of particles' lift-off velocities serve as an initial condition and significant quantities connecting the behavior of a single particle and that of wind-blown sand flux, so they have become key issues in the subject of wind-blown sand movement, especially after the International Conference on Aeolian Research hold in Aarhus, Denmark, 1986.

Common statistical methods include the orthogonal array method, the sampling test method, the histogram method, and the histogram method is the most widely applied method. Here, the equal distance histogram method is employed to calculate the probability distribution of lift-off velocities. First, all experiment data are collected as a sample space, and the region of velocities is equally divided into several subregions, then by calculating the number of velocities in each subregion, we can get the probability distribution of lift-off velocities. For example, experiments by Xie et al. (2007) show that the left/right spin angular velocities of sand particles range from 0 to 850 rev·s^{-1}, so the region (0 rev·s^{-1}, 850 rev·s^{-1}) is divided into 8 subregions with equal interval 100 rev·s^{-1}. By calculating the number of angular velocities in each subregion, we can get the probability distribution of left/right angular velocities shown in Fig. 3.11. Since the distributions of left and right angular velocities have the same form, we only give the distribution of left angular velocity. From Fig. 3.11, we can find that the distributions of both the left and right spin angular velocities are single-peaked and skewed, and most of the angular velocities are distributed in the region (150 rev·s^{-1}, 250 rev·s^{-1}).

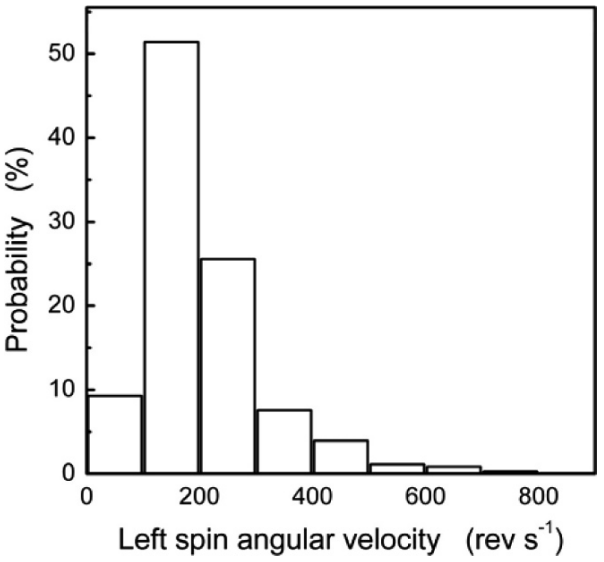

Fig. 3.11. Probability distribution of left angular velocities, analyzed by the equal distance histogram method on the basis of 1335 clear segments of saltation trajectories (from Xie et al. 2007)

Through the normalization method, that is, dividing the probability of each subregion by its interval, we can get the probability density distributions (PDFs) of lift-off velocities or angular velocities. With the aid of the theory of hypothesis testing (DeGroot and Schervish 2002), the corresponding PDFs can be determined.

For example, based on a wind tunnel experiment with Phase Doppler Anemometry (PDA), Xie et al. (2005) obtained the probability density function of lift-off velocities through a χ^2-test. They found it follows a Gamma function (Table 3.2). More existing probability density functions of lift-off velocity and its vertical component are listed in Table 3.2 and illustrated in Fig. 3.12, respectively. It can be found that there exist large discrepancies among the existing PDFs of lift-off velocities both in quality and quantity, which may result from the limitations of the experimental measurement.

Here, with the aid of the probability theory of multi-random variables (Bickel and Doksum 1977), we present a theoretical prediction of the PDF of lift-off velocities based on the analytical solutions of rebound and ejected velocities given in Eqs.3.20–3.25. For simplicity, only the two-dimensional ‘uniform’ case is illustrated.

Table 3.2. Several forms of existing PDFs of lift-off velocities

Authors (in publishing date)	Probability density function of lift-off velocities	Remark
Anderson and Hallet (1986)	$f(V)=\frac{1}{0.63u_*}\exp\left(-\frac{V}{0.63u_*}\right)$ $f(V)=\frac{(3V)^3\exp\left(-\frac{3V}{0.96u_*}\right)}{2(0.96u_*)^4}$	u_* represents the friction wind velocity
Nalpanis et al. (1993)	$f(V)=\frac{1}{\sigma_V V\sqrt{2\pi}}\exp\left[-\frac{(\ln(V)-\mu_V)^2}{2\sigma_V{}^2}\right]$	μ_V, $\sigma_V{}^2$ represent the mean and variance of lift-off velocities respectively
Zhu et al. (2001)	$f(V)=\frac{\exp\left(-\frac{V^2}{2A}\right)}{\sqrt{2\pi C}}$	A, C is parameters
Zou et al. (2001)	$f(V)=a+\frac{b}{1+4\frac{(H-c)^2}{d^2(2^{1/e}-1)^e}}$	H is the height from sand surface; a, b, c, d, e are parameters varying with the height
Xie et al. (2005)	$f(V)=\frac{\lambda_1^{\lambda_2}V^{(\lambda_2-1)}\exp(-\lambda_1 V)}{\Gamma(\lambda_2)}$	λ_1, λ_2 are parameters determined by the mean value and the variance of experiment data

Let $X_1, X_2,..., X_n$ be real random variables, $Y = Y(X_1, X_2,..., X_n)$ be a real function, and $Z = [Y, X_2,..., X_n]^T$ is a real transform from n-dimensional realspace $\Re^n$ to $\Re^n$. If Z satisfies the following conditions: (a) all first order partial differentials of Z are continuous in $\mathcal{B} \subseteq \Re^n$; (b) the transform between Z and X is a one-to-one mapping in $\mathcal{B} \subseteq \Re^n$ and (c) the Jacobian determinant $J_Z(\mathbf{X})$ is always not zero, then we can write the PDF $f_Y(Y)$ of random variable Y as follow:

$$f_Y(Y)=\int\cdots\int f_Z(Z)\mathrm{d}X_2\mathrm{d}X_3\cdots\mathrm{d}X_n=\int\cdots\int f_X(\mathbf{X})\left|\frac{1}{J_Z(\mathbf{X})}\right|\mathrm{d}\mathbf{X}, \tag{3.26}$$

in which $\mathbf{X} = [X_1, X_2,..., X_n]^T$ and $\int_Z |f(\mathbf{X})|\mathrm{d}\mathbf{X} < \infty$. Denoting $Y = V$ (V is taken as any component of lift-off velocity), $X_1 = V_A$, $X_2 = \alpha_k$, $X_3 = \beta$, $X_4 = \theta_0$ and $X_5 = V_B$ and employing the probability density distribution

given by Eqs. 3.6–3.9, the probability density of lift-off velocities can be derived from Eq. 3.26, that is:

$$f_{V_{Ax}}=\iiint\frac{f_{V_{A0}}f_{\theta_0}f_{V_{B0}}\left|9+\frac{4D_A^3}{D_B^3}[1+\sin(\alpha_k+\beta)][2-\sin(\alpha_k+\beta)]\right|}{(1+k_{12})\pi^2\left|3\cos\alpha_k+\sin\beta-2\sin\beta\sin(\alpha_k+\beta)\right|}d\theta_0 d\beta d\alpha_k dV_{A0}, \quad (3.27)$$

$$f_{V_{Az}}=\iiint\frac{f_{V_{A0}}f_{\theta_0}f_{V_{B0}}\left|9+\frac{4D_A^3}{D_B^3}[1+\sin(\alpha_k+\beta)][2-\sin(\alpha_k+\beta)]\right|}{(1+k_{12})\pi^2\left|3\sin\alpha_k+\cos\beta-2\cos\beta\sin(\alpha_k+\beta)\right|}d\theta_0 d\beta d\alpha_k dV_{A0}, \quad (3.28)$$

$$f_{V_{Bx}}=\iiint\frac{2f_{V_{A0}}f_{\theta_0}f_{V_{B0}}\left|9+\frac{4D_A^3}{D_B^3}[1+\sin(\alpha_k+\beta)][2-\sin(\alpha_k+\beta)]\right|}{\pi^2\left|6-3k_{12}-\frac{4k_{12}D_A^3}{D_B^3}[1+\sin(\alpha_k+\beta)][2-\sin(\alpha_k+\beta)]\right|\left|\cos\alpha_k\right|}d\theta_0 d\beta d\alpha_k dV_{A0}, \quad (3.29)$$

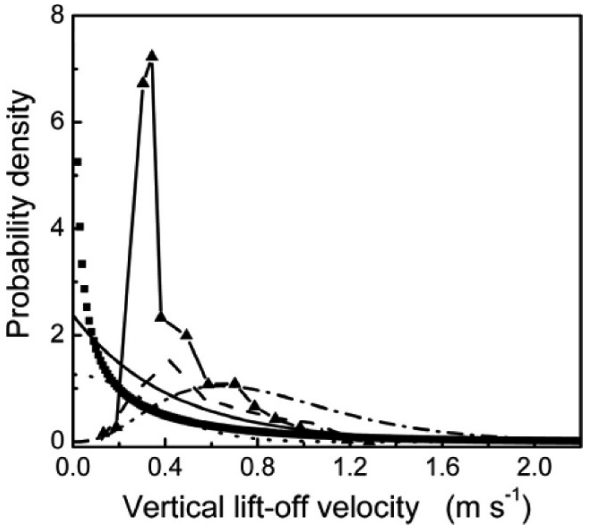

Fig. 3.12. Probability density function (PDF) of vertical lift-off velocities with shear wind velocity $u_* = 0.68$ m·s^{-1}. – – – – the measured results presented by Nalpanis et al. (1993), –▲– the measured results presented by Zou et al. (2001), ■ the theoretical results presented by Xie et al. (2005), ····· the theoretical results presented by Zhu et al. (2001), ——— the exponent curve fitted by Anderson and Hallet (1986), – · – · – the Gamma curve fitted by Anderson and Hallet (1986)

$$f_{V_{Bz}}=\iiint\frac{2f_{V_{A0}}f_{\theta_0}f_{V_{B0}}\left|9+\frac{4D_A^3}{D_B^3}[1+\sin(\alpha_k+\beta)][2-\sin(\alpha_k+\beta)]\right|}{\pi^2\left|6-3k_{12}-\frac{4k_{12}D_A^3}{D_B^3}[1+\sin(\alpha_k+\beta)][2-\sin(\alpha_k+\beta)]\right|\sin\alpha_k|}d\theta_0 d\beta d\alpha_k dV_{A0}, \quad (3.30)$$

$$f_{\omega_A}=\iiint\frac{D_A f_{V_{A0}}f_{\theta_0}f_{V_{B0}}\left|9+\frac{4D_A^3}{D_B^3}[1+\sin(\alpha_k+\beta)][2-\sin(\alpha_k+\beta)]\right|}{|4(1+k_{12})[1+\sin(\alpha_k+\beta)]|}d\beta d\theta_0 d\alpha_k dV_{A0}, \quad (3.31)$$

$$f_{\omega_B}=\iiint\frac{D_B f_{V_{A0}}f_{\theta_0}f_{V_{B0}}\left|9+\frac{4D_A^3}{D_B^3}[1+\sin(\alpha_k+\beta)][2-\sin(\alpha_k+\beta)]\right|}{6(1+k_{12})}d\beta d\theta_0 d\alpha_k dV_{A0}. \quad (3.32)$$

It is notable that from Eqs. 3.20–3.23, we can deduce the expression of creeping velocity V_{B0} and its corresponding components in terms of incident velocity V_{A0}, the incident angle θ_0, the impact angle β, and the contact angle α_k. Therefore, the expressions 3.27–3.32 do not integrate with V_{B0}.

Besides, using a numerical integration method, such as the Gaussian integration of 4 nodes, the rebound and ejected velocities for a given diameter of sand particle and wind velocity can be obtained. Taking the velocities with positive vertical component as sample space, we can get the corresponding probability density function (PDF). Fig. 3.13 gives the probability density distribution of horizontal and vertical lift-off velocities, and Fig. 3.14 gives the probability density distribution of angular velocities when the wind velocity is 8 $m \cdot s^{-1}$ and the diameter of sand particle is 0.35 mm.

It can be seen that the horizontal lift-off velocities follow a unimodal distribution, the vertical lift-off velocities follow a negative exponential distribution and the angular velocities follow an asymmetrical unimodal distribution. In addition, the range of rebound velocities is wider than that of ejected velocities, rebound angular velocities follow a Gumble distribution and ejected angular velocities follow a Gaussian distribution. Furthermore, wind velocity and the diameter of the sand particle affect the distributions of lift-off and angular velocities but do not change their type.

In practice, the lift-off sand particles include rebound and ejected ones, and the measured PDFs of lift-off velocities are of total lift-off particles including both rebound and ejected ones and are, however, difficult to identify by present experiments in a wind-blown sand flux. In order to get them from the theoretical predictions of these cases, we use the notations N_r, N_e and N_s represent the numbers of rebound, ejected and total lift-off

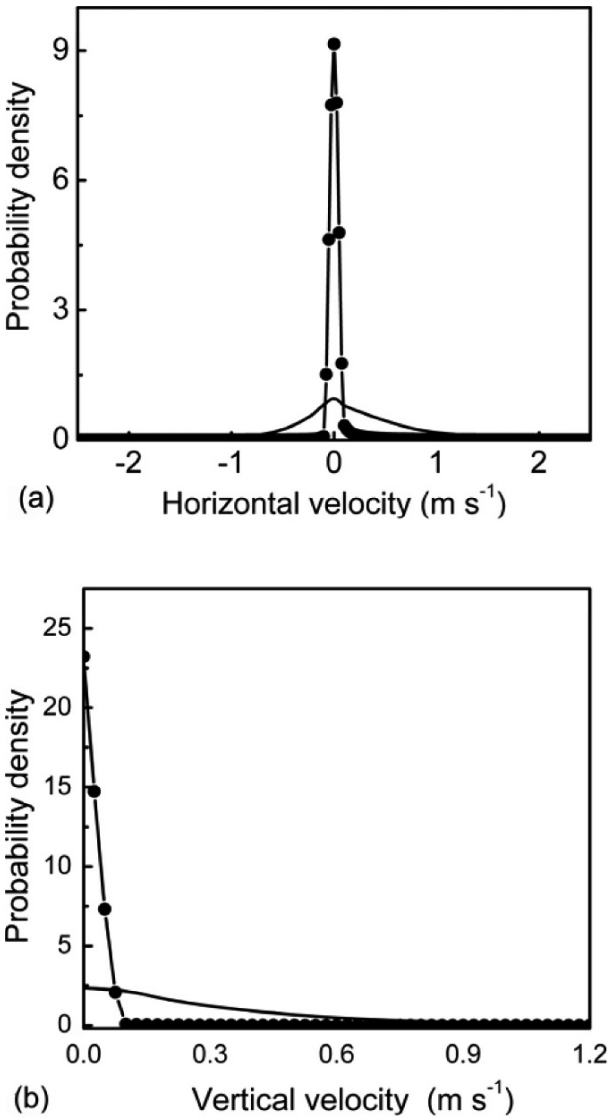

Fig. 3.13. The probability density distribution of **(a)** horizontal velocity and **(b)** vertical velocity of rebound and ejected sand particles when the wind velocity is 8 $m \cdot s^{-1}$ and the diameter of sand particle is 0.35 mm; —— the rebound components, –●– the ejected components (Zheng et al. 2005)

sand particles per unit area per unit time, respectively. They satisfy $N_s = N_r + N_e$. Denote $a_r = N_r / N_s$ and $a_e = N_e / N_s$, it is obviously that a_r and a_e stand for the fractions of rebound and ejected sand particles respec-

tively, and $a_r + a_e = 1$. Then we can write the PDF of lift-off velocities of total lift-off sand particles as follows:

$$f(V) = \lim_{\Delta V \to 0} \frac{N_r \int_V^{V+\Delta V} f^{(r)}(V)dV + N_e \int_V^{V+\Delta V} f^{(e)}(V)dV}{N_s \Delta V} = a_r f^{(r)}(V) + a_e f^{(e)}(V), \quad (3.33)$$

where ΔV is the interval of velocity subregion, and the recommended values for a_r and a_e are listed in Table 3.3 for different wind velocities and diameters of sand particle. A comparison between predictions made by the stochastic particle-bed collision model and experimental data on the PDF of vertical component is shown in Fig. 3.15. It can be seen that the results of the stochastic particle-bed collision model agree with the experimental data made by Dong et al. (2002), and are better than the results given by the other functions listed in Table 3.2, which verifies the reliability of the stochastic particle-bed collision model to some extent.

In addition, some researchers attempted to investigate the PDF of lift-off velocities through combining the traditional experimental measurements with theoretical predictions of sand flux and wind velocity profile (Huang et al. 2006). They first gave an initial PDF with several undetermined

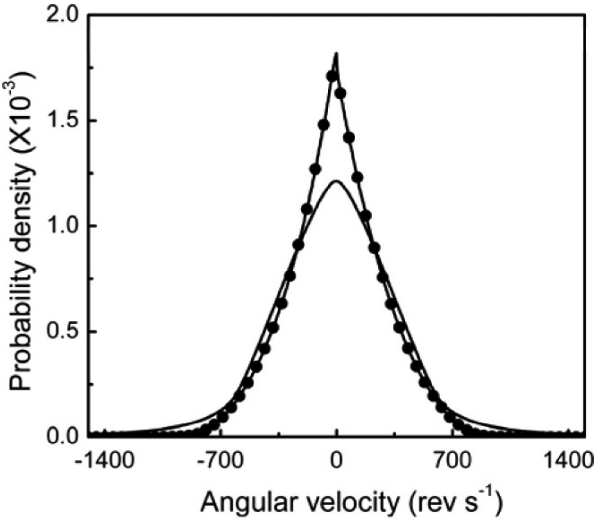

Fig. 3.14. The probability density distribution of rebound and ejected angular velocity when the wind velocity is 8 m·s^{-1} and the diameter of sand particle is 0.35 mm; —— the rebound components, –●– the ejected components (Zheng et al. 2006)

parameters, and numerically calculated the sand transport rate using the model of wind-blown sand movement (see Chap. 5), and then by adjusting the values of the pending parameters made all numerical results could be close to the experimental results, finally an optimization PDF could be obtained using an optimization method, such as the penalty function method. They obtained an exponential density function for vertical lift-off velocities of sand particles with respect to shear velocity.

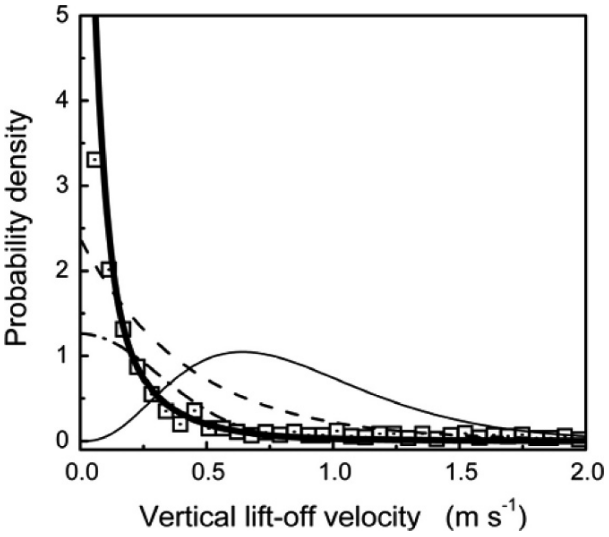

Fig. 3.15. Comparison of predictions and experimental data of the PDF of vertical component with $a_r = 0.87$ and $a_e = 0.13$. □ experimental results (Dong et al. 2002), ——— theoretical results (Zheng et al 2005), —— Gamma function, – – – exponent function and (Anderson and Hallet 1986) – • – • – Gauss function (Zhu et al. 2001)

Table 3.3. The values of a_r and a_e for different wind velocities and diameters of sand particles

Wind velocity [m·s^{-1}]	Diameter [mm]	a_r	a_e	Wind velocity [m·s^{-1}]	Diameter [mm]	a_r	a_e
8.0	0.25	0.93	0.07	12.0	0.35	0.94	0.06
10.0	0.25	0.93	0.07	14.0	0.35	0.945	0.055
12.0	0.25	0.94	0.06	8.0	0.45	0.84	0.16
14.0	0.25	0.955	0.045	10.0	0.45	0.96	0.04
8.0	0.35	0.87	0.13	12.0	0.45	0.94	0.06
10.0	0.35	0.9	0.1	14.0	0.45	0.92	0.08

The probability density functions of lift-off velocities discussed and presented in this section are all for steady wind fields. If the wind field is fluctuating, we can extend the above results by adjusting the friction wind velocities in Table 3.3 to instantaneous fluctuating values.

3.5 Splash Function

The splash function is an expression of the particle-bed collision process, which describes the mean number of sand particles (including rebound and ejected ones) rising from the bed surface subsequent to a single impact of a sand particle for a given velocity and particle diameter. It directly reflects the characteristics of momentum, energy and mass exchange between the incident particle and the bed surface and serves as a bridge crossing the microscopic behavior of a single particle to the macroscopic wind-blown sand movement. Existing splash functions have two basic types. One is to present the mean number of sand particles jumping from the bed per impact for a given impact velocity V_{im} and impact diameter D_{im}, namely the integral-type splash function $\bar{N}_{ej}(V_{im}, D_{im})$, the other is to give out the rebound probability $N_r(V_j, V_{im}, D_{im})$ and the number of ejected particles $N_e(V_j, V_{im}, D_{im})$ leaving the bed in velocity bin V_j with a given V_{im} and D_{im}, namely the discrete-type splash function. As we introduced in Sect. 3.2, a general description of the collision process and the splash function can be obtained on the basis of direct observation. However, because of the dense concentration within the layer under 0.5 cm height, only those distinguishable and slow-moving particles can be identified. Therefore, the observation results cannot draw a comprehensive understanding of the particle-bed collision process. In order to remedy these limitations, some researchers attempt to simulate the whole particle-bed collision process with the aid of computer simulation, which can accurately monitor the motion of every sand particle, and hence reflect the character of particle-bed collision in quality and reveal the splash function and the PDF of lift-off velocities in quantity. Here, we briefly introduce the results of splash functions through the DEM simulation for 'uniform' sands and 'mixed' sands.

3.5.1 Splash Function for 'Uniform' Sands

Werner and Haff (1988) made two-dimensional simulations for ordered packing of beads using a discrete element method. The particle-bed collisions were simulated by propelling a single particle into a bed of 384 circular particles with diameter of 1 cm. The interaction forces between parti-

cles have been modeled as follows. The normal force is described as a stiff damped oscillator and the shear force as well, except that it is limited by the usual friction force. In particular, he was able to extract a law for the normal restitution coefficient for the impacting bead e_z, which is independent from the impacting speed. He also found that the ejected particles acquired roughly 1–20% of the incident velocity, and established an integral-type splash function as a function of the incident angle θ_{im} and incident speed V_{im}:

$$\bar{N}_{ej}\left(\theta_{im}, V_{im}\right) = 3.36\left(0.572V_{im} - 0.915\right)\sin\theta_{im} \tag{3.34}$$

where $\bar{N}_{ej}$ is the mean number of ejected particles.

Anderson and Haff (1988) performed two-dimension simulations of single-grain impacts into a granular bed with 87 identical slightly inelastic, 1 mm-diameter grains to evaluate the splash process quantitatively. Interactions between grains were characterized by a coefficient of restitution, an inter-grain friction coefficient, and an elastic modulus. The simulations were performed by dropping 8 particles with random initial velocities into a box with periodic boundaries, whose width was chosen such that the resulting bed was about ten grains deep. Three such granular beds with different packing configurations were used and each of them was impacted 20 times to develop the splash statistics for each impact angle and speed. The results showed that the mean rebound speed is approximately 50% to 60% of the impact velocity, and the mean rebound angle is 30° to 40° from the horizontal. The mean speed of the ejected particles appears to saturate at 9%–10% of the speed of the impacting grain, and the mean ejection angle tends to oriented downwind at 60° to 70° from the horizontal, the mean number of grains ejected increases roughly linearly with impact velocity. Later, Anderson and Haff (1991) conducted simulations of 20 impacts into a bed of 500 identical spheres using more typical aeolian sand sizes: $D_s = 0.23$ mm and $D_s = 0.32$ mm. The impact angles and speeds were chosen to cover the ranges typical of aeolian saltation impacts in air (angles 8°–15°; speeds 0.25–8 $\mathrm{m{\cdot}s^{-1}}$) with the number of impacts as 20 for each case. Their results suggest that for the chosen grain parameters, the mean rebound speed, ejected speed and the mean number of ejected particles all increase with the impact velocity. The rebound speed is approximately 50%–60% of the impact velocity, the mean rebound angle is 35°–45° from the horizontal; and the mean ejected speed is roughly 9%–10% of the impact velocity. Based on their simulations, they present a discrete-type splash function:

$$N_r\left(V_j\right) = N_{r0}\exp\left(-\frac{V_j - bV_{im}}{cV_{im}^2}\right)dV \tag{3.35}$$

$$N_e\left(V_j\right) = N_{e0}\exp\left(-\frac{V_j}{hV_{im}^k}\right)dV \tag{3.36}$$

where $N_{r0} = 0.95$, $N_{e0} = (1.75\ V_{im})^{1.0}$, $b = 0.56$, $c = 0.2$, $h = 0.25$ and $k = 0.3$. In each case $dV = 0.1\ \mathrm{m{\cdot}s^{-1}}$ which is the width of the ejection velocity bin. $N_r\,(V_j)$ and $N_e\,(V_j)$ represent the number of rebound and ejected grains leaving the bed in the j-th ejection velocity bin, labelled V_j, subsequent to a single impact of velocity V_{im}. Distribution of rebound and ejected particles can be fitted by a Gaussian distribution and exponential function respectively. Further, Haff and Anderson (1993) employed the soft-particle approach to simulate the particle-bed collisions in wind-blown sand flux. In their simulation, an initial bed containing 500 grains was prepared, with approximately 33% of the particles of diameter 0.0328 cm and 67% of diameter 0.0231 cm. In particular, a 'particle cooling' technique was used to speed up the bed generation process, that is, firstly the grains were given random velocities and allowed to fall under the influence of gravity, which made the granular system initially have a significant kinetic energy due to the grains' motion, later, it will be artificially converted into a state in which all particle velocities are set equal to zero so as to set up a convenient bed as economically as possible. Besides, they investigated the dependence of the splash pattern on variations of particle properties, such as the spring constant and the coefficient of restitution. These results contributed a lot to the further application of the DEM in granular systems and sediment transport systems.

Based on the work of Haff and Anderson (1993), Xie (2005) performed similar simulations to investigate the influence of sand particle diameter on the splash process characteristic. 12 impacts were run for sand particles with diameters ranging from 0.1 mm to 0.5 mm, and the results showed that except for the impact velocity V_{im} the diameter of sand particles also has a significant influence on the splash function (Fig. 3.16). Since in 'uniform' sand case, the impact particle and the particles on the bed have the same diameter, we denote the diameter of sand particle as D_{bed} for simplicity. Then the integral-type splash function given in Xie (2005)'s doctoral dissertation can be expressed as:

$$\bar{N}_{ej} = C_1 + C_2 V_{im}\,, \tag{3.37}$$

where C_1=–99.708D_{bed}^2+81.391D_{bed}–15.146 , C_2=110.665exp$\left(-D_{bed}/0.047\right)$ +1.555.

Since the impact velocity V_{im} is believed to be a random variable, the mean number of ejected sand particles $\overline{N}_{ej}$ is also supposed to be a random variable. Denoting the distribution of $\overline{N}_{ej}$ by F_{Ne} (n_e), it can be written as

$$F_{N_e}\left(n_e\right)=P\left(N_e<n_e\right), \tag{3.38}$$

where P ($N_e < n_e$) represents the probability of the case that the mean number of ejected particles is less than n_e. Substituting Eq. 3.38 into Eq. 3.37, we get

$$F_{N_e}=P\left(C_1+C_2V_{im}<n_e\right)=P\left(V_{im}<\frac{n_e-C_1}{C_2}\right)=F_{V_{im}}\left(\frac{n_e-C_1}{C_2}\right). \tag{3.39}$$

Therefore, for a given probability distribution of impact velocities, such as the one given by Dong et al. (2002), the probability density of the number of lift-off sand particles can be expressed as:

$$f_{N_e}=f_{V_{im}}\left(\frac{n_e-C_1}{C_2}\right). \tag{3.40}$$

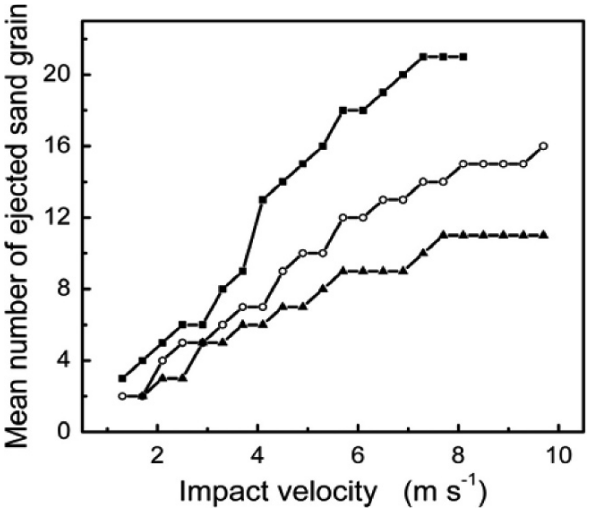

Fig. 3.16. The mean number of ejected particles versus impact velocity for several particle diameters; –■– for particle diameter 0.23 mm, –○– for particle diameter 0.34 mm and –▲– for particle diameter 0.46 mm (Xie 2005)

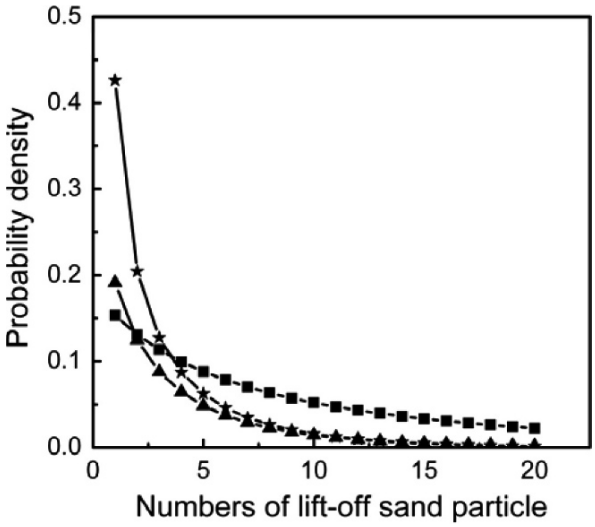

Fig. 3.17. The effect of particle diameter on the probability density of the number of lift-off sand particles with wind velocity 7.0 $m \cdot s^{-1}$; –■– for particle diameter 0.15 mm, –▲– for particle diameter 0.20 mm and –★– for particle diameter 0.25 mm (Xie 2005)

Since parameters C_1 and C_2 are functions of sand diameter D_{bed} and impact velocity V_{im} is related to wind velocity, the probability density of the number of lift-off sand particles, the so-called number density, is supposed to be a function of wind velocity and sand diameter.

Fig. 3.17 illustrates the number density of lift-off sand particles for diameter 0.15 mm, 0.2 mm and 0.25 mm, respectively. It can be seen that for a given wind velocity the probability density curve becomes steeper when the particle diameter is larger, in other words, larger sand particles are less susceptible to being ejected under the impact of sand particles of the same size. From a comparison of the probability densities of the sand particles with a diameter of 0.25 mm under wind velocity 8.0 $m \cdot s^{-1}$, 12.0 $m \cdot s^{-1}$ and 15.0 $m \cdot s^{-1}$, we can conclude that the effect of wind velocity is negligible.

3.5.2 Splash Function for 'Mixed' Sands

Although the effect of the particle diameter on the splash process has been mentioned in the studies mentioned above, most of these investigations are limited to 'uniform' sand case, which cannot give a realistic description of natural particle-bed collision. In order to acquire an understanding of grain collisions in wind-blown sand movement, it is necessary to simulate the

stochastic collisions on a sand bed composed of 'mixed' sand particles. The simulation procedures can be taken as follows:

Step 1: Generation of a 'mixed' sand bed. In order to simulate natural sand particle-bed collision, one of important steps for us is to generate a 'mixed' sand bed with randomly distributed particle size of the same diameter distribution as that obtained in field measurements. A periodic rectangular box is taken to be of length L_b and height H_b, the sizes of the N particles in the bed are chosen to fit the distribution of natural sand; and the bottom of the box is covered by an array of large particles which are assumed to be immobile during the simulation. The particles fall down to the bed with random positions $X_i\,(x_i,\ z_i)$ and velocities $V_i(V_{x_i}, V_{z_i})$ ($i = 1, 2, ..., N_b$). Due to the inelasticity of grain collisions, the total kinetic energy of the granular system decreases with time and the system finally develops into a 'natural' bed with particles of varying sizes.

Step 2: Contact detection. After the selection of impact velocity V_{im}, impact diameter D_{im}, and impact points on the bed, we need to deal with the particle-particle interaction between neighboring particles. Over the course of each particle-bed collision event, a series of 'chain reaction' are initiated by the impact particle. That is, any two particles may in principle eventually come into contact, even though initially they may be far apart. Therefore, an additional computational issue is the detection of contacts between neighboring grains.

Step 3: Calculating the motion of each particle. From the contact detection in Step 2, we can establish a 'neighbor list' for each particle in the system, and sequentially obtain the velocity and position of each particle by solving the equations of motion based on the soft-particle or hard-particle approach presented in Sects. 3.3.2 and 3.3.3.

Step 4: Collecting the rebound and ejected particles. Repeat the calculations from step 2 to step 3 until the incident particle rebound from the bed surface, and then collect the lift-off velocity V_e of ejected particles.

After performing simulations for each combination of sand diameter and impact velocity, we can find some possible regions of variables, denoted by $V_{ej} \in [0, V_{ej}^{\max}]$. Dividing the region into k^* subregions and calculating the number of rebound and ejected particles in each subregion, we can get the discrete-type splash function

$$N_{rD}\left(V_j\right) = 0.85\exp\left[-\frac{\left(V_j - \mu_{rD}\right)^2}{2\sigma_{rD}{}^2}\right], \qquad N_{eD}\left(V_j\right) = A\exp\left(-BV_j\right). \quad (3.41)$$

For discrimination, subscript D is used to represent the mean diameter of the sand bed particles; N_{rD} and N_{eD} represent the probability of rebound

and ejected particles; A, B, μ_{rD}, σ_{rD} are fitting parameters. For the width of velocity subregion taken as 0.1 m·s^{-1}, they can be written as follows, respectively,

$$A = 0.02V_{im}\left(V_{im} + 150D_{im} - 15\right) + D_{im}\left(8.3D_{im} - 4\right),$$

$$B = 0.02D_{im}\left(D_{im} + V_m - 37.5\right) - 0.15V_{im}\left(V_{im} - 5.87\right) + 1.44,$$

$$\sigma_{rD} = V_{im}\left(0.04V_{im} - 0.7D_{im} + 0.14\right) + 0.4D_{im} - 0.1,$$

$$\mu_{rD} = 9D_{im} + 0.65V_{im} - 0.16.$$

It is worth noting that Eq. 3.41 is a statistical result based on simulations of a sand bed with 4000 particles of varied size, in which 10 groups of representative diameters: 0.09 mm, 0.12 mm, 0.14 mm, 0.16 mm, 0.18 mm, 0.19 mm, 0.2 mm, 0.21 mm, 0.28 mm and 0.45 mm are selected to construct the 'natural' bed, with corresponding volume percentage being 0.095%, 0.13%, 12.58%, 31.54%, 27.69%, 15.83%, 7.47%, 3.22%, 1.33% and 0.11%, respectively. The resulting sandy bed is of 4.5 cm length, 0.45 cm height. The mean particle diameter of the whole bed and the surface layer are 0.203 mm and 0.22 mm respectively.

Comparing the discrete-type splash function given by Anderson and Haff (1991) and Eq. 3.41 (see Fig. 3.18), we can find for the same impact velocity V_{im}, if the impact diameter D_{im} is equal to the mean diameter D, both the ejection speed and the ejection number in the 'mixed' sand case are a little larger than those in 'uniform' sand case; if the impact diameter D_{im} is larger than the mean diameter D, the discrepancy becomes much higher. It is because in 'mixed' sand case, the small sand particles near the impact position are easier to be ejected when the impact velocity reaches a certain value. While in the 'uniform' sand case, the sand particles near the impact position have the same diameter as the impact particle, which makes them less easily to be ejected.

Summing over all possible ejection speed subregions, we get the integral-type splash function for 'mixed' sands:

$$\bar{N}_{ej} = V_{im}\left(0.08V_{im} + 7.1D_{im} - 1.2\right) + D_{im}\left(33.3D_{im} - 16.1\right). \tag{3.42}$$

Comparison between the results of Eq. 3.42 and other integral-type splash functions are shown in Fig. 3.19, in which the results calculated by Eqs. 3.36 and 3.37 are proposed by Anderson and Haff (1991) and Xie et al. (2005) for a 'uniform' sand bed respectively. Zhou et al. (2006) presented

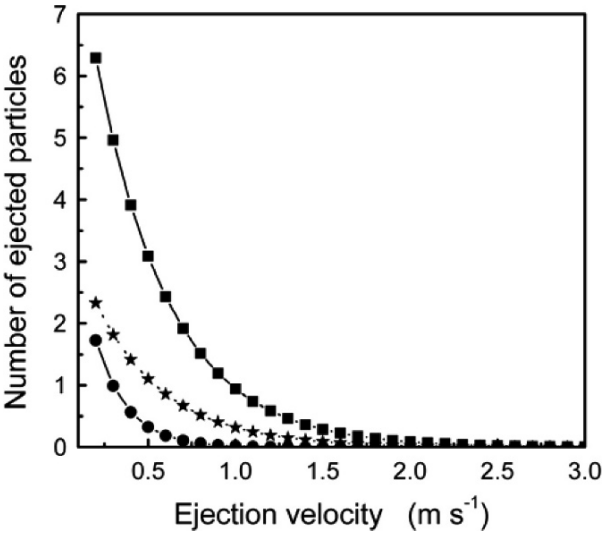

Fig. 3.18. Comparison between the results of discrete-type splash functions; –●– the results calculated by Eq. 3.36 for 'uniform' sand case (D_{im}=0.32 mm), –★– the results given by Eq. 3.41 for 'mixed' sand case (D_{im}=0.32 mm), –■– the results given by Eq. 3.41 for 'mixed' sand case (D_{im}=0.5 mm)

an integral-type splash function for 'mixed' sands through their simulations on a 'mixed' sand bed with mean diameter 300 um. Their results can be written as follow:

$$\overline{N}_{ej} = 17.96 + 18.05 \ln\left(0.37 + \frac{1}{6} D_{im}^3 \pi \rho_s V_{im}\right). \tag{3.43}$$

From Fig. 3.18, we can find that either for 'uniform' sand case or 'mixed' sand case, the mean ejection number increases with the impact velocity. Quantitatively speaking, the results of the 'mixed' sand case get close to the results of the 'uniform' sand case for an impact diameter of 300 um which is the same as the diameter of the 'uniform' sand bed when impact velocity is lower than 5 m·s^{-1}, after that, results given by Eq. 3.42 are a little higher while those given by Eq. 3.43 are a little lower than the results of the 'uniform' sand case. This mainly arises from the fact that particles larger than 300 um on the sand bed employed in Zhou et al. (2006) form a considerable percentage of the number ejected which are less easily ejected compared with the 'uniform' sand case. Besides, from the comparison between the results of two 'mixed' cases, we can also find that the mean ejection number subsequent to the impact of sand particles of

500 μm is larger than that of 300 μm (which is equal to the mean particle diameter of the sand bed). Specifically, the results calculated by 3.41 are lower than those calculated by 3.42 for $V_{im} < 8$ m·s^{-1}, while the latter are higher than the former for $V_{im} > 8$ m·s^{-1}. This is also a result of different size distribution of the sand bed employed in the numerical simulation.

It is notable that by applying the above method, we can also obtain information about the lift-off velocities of sand particles. For example, Zhou et al. (2006) concluded that for a given diameter and impact velocity, the mean ejection velocity follows the relation,

$$\overline{V}_e = 0.43 + 0.077 \ln\left(0.029 + \frac{1}{6} D_{im}^3 \pi \rho_p V_{im}\right). \tag{3.44}$$

Taking all of the sand particles lifting from the sand bed in the simulations as a sample space the probability distribution of lift-off velocities for

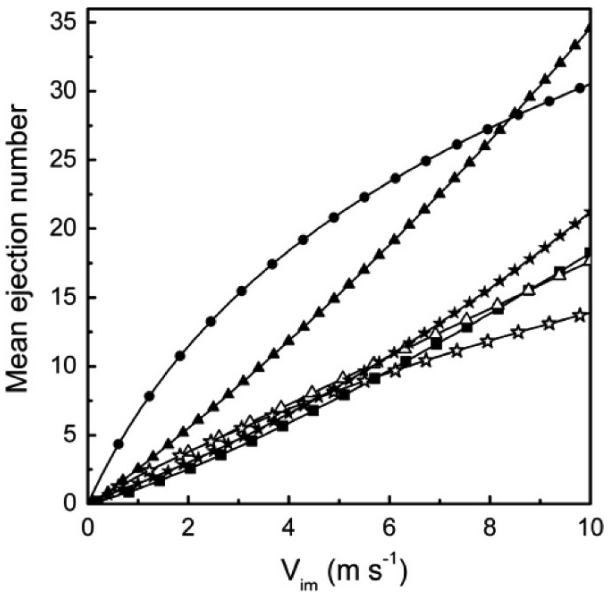

Fig. 3.19. Comparison of the results of existing integral-type splash functions for 'uniform' sand case and 'mixed' sand case; –■– the results calculated by Eq. 3.36 for 'uniform' sand case (D_{bed} = 0.32 mm), –△– the results calculated by Eq. 3.37 for 'mixed' sand case (D_{bed} = 0.3 mm), –☆– the results calculated by Eq. 3.43 for 'mixed' sand case (D_{in} = 0.3 mm) –●– the results calculated by Eq. 3.43 for 'mixed' sand case (D_{in} = 0.5 mm), –★– the results calculated by Eq. 3.42 for 'mixed' sand case (D_{in} = 0.3 mm), –▲– the results calculated by Eq. 3.42 for 'mixed' sand case (D_{in} = 0.5 mm)

a given shear velocity can be obtained. Fitting all sets of the numerical results of particle-bed collision with the least squares method, the PDF of vertical, downwind and upwind horizontal and resultant velocities follow an exponential function as follow,

$$f(V,u_*) = A\exp\left[-A\left(|V| - V_{cr}\right)\right], \tag{3.45}$$

where V represents vertical, downwind and upwind horizontal or resultant velocities; V_{cr} is the threshold starting velocity of a sand particle, which is proved to be a constant approximately for any shear wind velocity; A (> 0) is a function of shear wind velocity u_* and it represents the probability of a sand particle launching with low velocity. Results fitted by the least squares method are shown below:

$$A_V = 8.66359 + \frac{0.72975}{0.33586\sqrt{0.5\pi}}\exp\left[-2\left(\frac{u_* - 0.6672}{0.33586}\right)^2\right], (V_{cr})_V = 0.0324 \tag{3.46a}$$

$$A_{V_y} = 2.66168 + \frac{0.19333}{0.18352\sqrt{0.5\pi}}\exp\left[-2\left(\frac{u_* - 1.03772}{0.18352}\right)^2\right], (V_{cr})_{V_y} = 0.2237 \tag{3.46b}$$

$$A_{V_{x-}} = 18.5185, \qquad (V_{cr})_{V_{x-}} = -0.0895 \tag{3.46c}$$

$$A_{V_{x+}} = 2.31227 + \frac{0.14236}{0.23775\sqrt{0.5\pi}}\exp\left[-2\left(\frac{u_* - 1.01733}{0.23775}\right)^2\right], (v_{cr})_{V_{x+}} = 0.5236 \tag{3.46d}$$

where V, V_y, V_{x-} and V_{x+} are resultant, vertical, upwind horizontal and downwind horizontal lift-off velocities of sand particles, respectively. Substituting Eq.3.44 into Eq. 3.43 we get the PDFs of resultant, horizontal and vertical lift-off velocities in a 'mixed' wind-blown sand flux, where the sand particle diameters follow log-normal distribution shown as in Fig. 3.1. The PDF for angular velocities of sand particles can be formulated in the same way as:

$$f(\omega,u_*) = \frac{0.8727}{(205.8 + 2.2u_*)\sqrt{0.5\pi}}\exp\left[-2\left(\frac{\omega + 0.4693}{205.8 + 2.2u_*}\right)^2\right] \tag{3.47}$$